

Supporting Information for:

A Thermally Stable {FeNO}⁸ Complex: Properties and Biological Reactivity of Reduced MNO Systems

Ashis K. Patra,[†] Koustubh S. Dube,[†] Brian C. Sanders,[†] Georgia C. Papaefthymiou,[€] Jeanet Conradie,^{‡,§} Abhik Ghosh,[‡] and Todd C. Harrop^{*,†}

[†]Department of Chemistry, The University of Georgia, Athens, Georgia 30602,

[€]Department of Physics, Villanova University, Villanova, Pennsylvania 19085,

[§]Department of Chemistry, University of the Free State, 9300 Bloemfontein, Republic of South Africa, and [‡]Department of Chemistry and Center for Theoretical and Computational Chemistry, University of Tromsø, N-9037 Tromsø, Norway

*E-mail: tharrop@uga.edu

<u>Contents:</u>	<u>Page:</u>
<u>General Information</u>	S4
<u>Physical Methods</u>	S5-S6
<u>Experimental/Spectroscopic Details</u>	S6-S21
Figure S1. X-band EPR spectra of [Fe(LN ₄)(NO)] 1 and 1 - ¹⁵ NO	S9
Figure S2. Cyclic voltammograms of 1 in MeCN	S10
Figure S3. Cyclic voltammograms of [Co(LN ₄)(NO)] (2) in MeCN	S10
Figure S4. FTIR spectra of 1 and 1 - ¹⁵ NO in a KBr matrix	S11
Figure S5. ¹⁵ N NMR spectrum of 2 - ¹⁵ NO in THF- <i>d</i> ⁸	S13
Figure S6. FTIR spectra of 2 and 2 - ¹⁵ NO in a KBr matrix	S14
Figure S7. ¹⁵ N NMR spectrum of [Co(Cp*) ₂][Fe(LN ₄)(NO)] (3) in CD ₃ CN	S16
Figure S8. ¹ H NMR spectrum of 3 in CD ₃ CN	S17
Figure S9. High resolution FT-ICR-MS of 3 and 3 - ¹⁵ NO	S18
Figure S10. FTIR spectra 3 and 3 - ¹⁵ NO in a KBr matrix	S19
Figure S11. UV-vis spectrum of 3 in MeCN at 298 K and changes over time	S20
Figure S12. UV-vis spectral decay of 3 in buffer at 298 K	S21
Figure S13. FTIR spectra (KBr) disproportionation products of 3 and 3 - ¹⁵ NO	S21
<u>Reactivity: Reaction with metmyoglobin (metMb)</u>	S22-S30
Figure S14. UV-vis of metMb before and after addition of 2 in buffer (pH 7.2)	S25
Figure S15. UV-vis of metMb before and after addition of 3 in buffer (pH 7.2)	S25
Figure S16. UV-vis of metMb and GSH before and after addition of 3 in buffer (pH 7.2)	S26
Figure S17. UV-vis of metMb, reduction to deoxyMb with sodium dithionite, and after addition of 3 in buffer (pH 7.2)	S27

Figure S18. UV-vis of metMb, reduction to deoxyMb with sodium dithionite, and after addition of 1 in buffer (pH 7.2)	S27
Figure S19. UV-vis of metMb after addition of 3 (1 mol-equivs) in buffer (pH 7.2)	S28
Figure S20. UV-vis of metMb after addition of 3 (3 mol-equivs) in phosphate buffer (pH 7.2)	S29
Figure S21. Plot of Absorbance at 422 nm vs. {FeNO} ⁸ mol-equivs	S30
<u>X-ray Crystallographic Data</u>	S31-S34
Table S1. Summary of crystal data for 1 and 2	S32
Table S2. Selected bond distances and bond angles for 1 and 2	S33
Figure S22. ORTEP views of the two independent molecules in the asymmetric unit of 1	S34
Figure S23. ORTEP view of 2	S34
<u>Computational Data</u>	S35-S45
Figure S24. Geometry optimized (OLYP/TZP) structure for the anion of 3	S36
Table S3. Optimized OLYP/TZP geometry parameters for 1 , 2 , and 3	S37
Table S4. Mulliken charges and spin populations for 1 , 2 , and 3	S38
Figure S25. OLYP/TZP {FeNO} ⁷ and {CoNO} ⁸ bending potentials	S38
Figure S26. Metal(d)-NO(π^*) in the three HOMO's of 1 , 2 , and 3	S39
Tables S5-S10. Optimized coordinates for 1-3	S40-S45
<u>Mössbauer Spectral Studies</u>	S46-S48
Figure S27. Zero-field Mössbauer spectrum of [Fe(LN ₄)(NO)] (1)	S47
<u>References</u>	S49-S50

Experimental Details

General Information. All reagents were procured from commercial suppliers and used as received unless otherwise noted. Research grade nitric oxide gas, NO(g), UHP, 99.5%) was obtained from Matheson Tri-Gas. The NO(g) was purified by passage through an Ascarite II[®] (sodium hydroxide-coated silica, purchased from Aldrich) column and handled under anaerobic conditions. ¹⁵NO(g) (¹⁵N, ≥ 98%) was purchased from Cambridge Isotope Laboratories and used without further purification. Equine skeletal muscle myoglobin (Mb) was purchased from Sigma-Aldrich and used as received. Acetonitrile (MeCN), methylene chloride (CH₂Cl₂), tetrahydrofuran (THF), diethyl ether (Et₂O), and pentane were purified by passage through activated alumina columns using an MBraun MB-SPS solvent purification system and stored over 4 Å molecular sieves under a dinitrogen (N₂) atmosphere before use. *N,N*-dimethylformamide (DMF) was purified with a VAC solvent purifier containing 4 Å molecular sieves and was stored under similar conditions. Anhydrous MeOH and EtOH were obtained by distilling the alcohol from Mg(OR)₂ (R = Me for MeOH, Et for EtOH) and under N₂. Toluene was purified by stirring overnight with 3 Å molecular sieves, distilled from CaH₂, and stored over 3 Å molecular sieves. All solvents were filtered to remove sieves with a 0.45 µm nylon filter immediately before use. The Fe(II) and Co(II) starting salts, (Et₄N)₂[FeCl₄] and (Et₄N)₂[CoCl₄] were prepared according to the published procedure.¹ All reactions were performed under an inert atmosphere of N₂ using standard Schlenk-line techniques or in an MBraun Labmaster glovebox under an atmosphere of purified N₂. All reactions and measurements involving NO(g), Fe-NO or Co-NO compounds were performed in the dark with minimal light exposure by wrapping the reaction flasks/vials with aluminum foil to avoid any potential photochemical reaction.

Physical Methods. FTIR spectra were collected with a ThermoNicolet 6700 spectrophotometer running the OMNIC software. Samples were run as solids via an ATR diamond transmission window or as KBr pellets in a stream of dry N₂. Solution FTIR spectra were obtained using a demountable airtight liquid IR cell from Graseby-Specac with CaF₂ windows and 0.1 mm spacers. All FTIR samples were prepared inside a glovebox under an inert atmosphere of purified N₂. The closed liquid cell was taken out of the box and spectra were acquired immediately. Solid-state magnetic susceptibility measurements were performed with a Johnson Matthey magnetic susceptibility balance at the recorded temperature. Solution-state susceptibility measurements were performed in solution at 298 K using the Evans method on a Varian Unity Inova 500 MHz NMR spectrometer.² X-band (9.60 GHz) EPR spectra were obtained on a Bruker ESP 300E EPR spectrometer controlled with a Bruker microwave bridge at 10 K. The EPR was equipped with a continuous-flow liquid He cryostat and a temperature controller (ESR 9) made by Oxford Instruments Inc. Electronic absorption spectra were run at 298 K using a Cary-50 UV-vis spectrophotometer containing a Quantum Northwest TC 125 temperature control unit. The UV-vis samples were prepared anaerobically in gas-tight Teflon-lined screw cap quartz cells with an optical pathlength of 1 cm. Electrochemistry measurements were performed with a PAR Model 273A potentiostat using a non-aqueous Ag/Ag⁺ (0.01 M AgNO₃/0.1 M ⁿBu₄NPF₆ in CH₃CN) reference electrode, Pt-wire counter electrode, and a Glassy Carbon working milli-electrode (diameter = 2 mm) under an Ar atmosphere. Measurements were performed at ambient temperature using 2.0-4.0 mM analyte in various solvents containing 0.1 M ⁿBu₄NPF₆ as the supporting electrolyte. Ferrocene (Fc) was used as an internal standard and all potentials are reported relative to the Fc/Fc⁺ couple ($E_{1/2}$ = 0.094 V in MeCN versus the prepared Ag/Ag⁺ reference electrode). Differential pulse voltammetry (DPV) was performed

with a potential increment of 2.0 mV, a pulse amplitude of 25 mV, a pulse width of 50 ms, and a pulse period of 100 ms. ^1H and ^{13}C NMR spectra were recorded in the listed deuterated solvent on a 400 MHz Bruker BZH 400/52 NMR spectrometer or a Varian Unity Inova 500 MHz NMR at 298 K with chemical shifts referenced to TMS or residual protio signal of the deuterated solvent. Low resolution ESI-MS data were collected on a Perkin Elmer Sciex API I Plus quadrupole mass spectrometer whereas high resolution ESI-MS data were collected using a Bruker Daltonics 9.4 T APEXQh FT-ICRM. Elemental microanalysis for C, H, and N were performed by QTI-Intertek (Whitehouse, NJ) or Columbia Analytical Services (Tucson, AZ).

Synthesis of compounds

(N^1E, N^3E)- N^1, N^3 -bis((1H-pyrrol-2-yl)methylene)propane-1,3-diamine (LN₄). To a batch of 1.442 g (19.45 mmol) of 1,3-diaminopropane dissolved in 2 mL of dry MeCN was added 3.692 g (38.82 mmol) of pyrrole-2-carboxaldehyde dissolved in 6 mL of dry MeCN in the presence of 4 Å molecular sieves (15% w/v) under an N₂ atmosphere. No apparent color change was observed. After stirring the reaction mixture at 40 °C for 2 h under N₂, a white precipitate was observed and the reaction was allowed to stir for another 2 h at RT. The insolubles (product and sieves) were filtered through a fritted glass funnel and washed thoroughly with MeCN. The product was then redissolved in 50 mL of CH₂Cl₂, filtered to separate the sieves, and the filtrate was concentrated on a rotary evaporator to afford a white powder (3.209 g, 14.06 mmol, 72%). mp: 118-120 °C. ^1H NMR (400 MHz, CDCl₃, δ from TMS): 8.04 (s, 1H, CH=N), 6.87 (s, 1H, Ar-H), 6.46 (d, 1H, Ar-H), 6.23 (t, 1H, Ar-H), 3.59 (t, 2H, CH=N-CH₂), 1.97 (p, 1H, CH₂-CH₂-CH₂). ^{13}C NMR (100.6 MHz, CDCl₃, δ from TMS): 152.10 (CH=N), 130.48 (Ar-C), 121.99 (Ar-C), 114.22 (Ar-C), 109.89 (Ar-C), 58.54 (CH=N-CH₂), 32.75 (CH₂-CH₂-CH₂). FTIR (ATR-

diamond, solid), ν_{\max} (cm^{-1}): 3111 (w), 3046 (w), 2941 (m), 2847 (m), 2746 (w), 1633 (vs, C=N), 1440 (w), 1417 (m), 1360 (w), 1340 (w), 1313 (w), 1246 (w), 1136 (w), 1125 (w), 1096 (w), 1062 (m), 1033 (m), 1024 (m), 988 (m), 968 (w), 959 (w), 919 (w), 881 (m), 789 (m), 743 (s), 656 (w), 607 (m). LRMS-ESI (m/z): $[\text{M} + \text{H}]^+$ calcd for $\text{C}_{13}\text{H}_{17}\text{N}_4$, 229.1; found, 229.0.

(Et₄N)₂[Fe(LN₄)Cl₂]. To a batch of LN₄ (0.6840 g, 2.996 mmol) dispersed in 5 mL of dry MeCN was added a 3 mL MeCN slurry of NaH (0.1480 g, 6.167 mmol), which resulted in H₂(g) evolution and a light purple-colored solution indicative of ligand deprotonation. To ensure complete deprotonation, an occasional vacuum was applied while stirring the solution further for ~15 min. To this solution was then added a 10 mL MeCN solution of (Et₄N)₂[FeCl₄] (1.372 g, 2.995 mmol) resulting in formation of a white precipitate (NaCl) and a pale orange-colored solution. The reaction mixture was stirred for another 2 h at RT, which resulted in no further change. Finally, the solution was filtered (0.315 g of insolubles, mostly NaCl) to obtain a clear orange-red filtrate that was evaporated to yield a gummy orange solid (1.782 g, 2.905 mmol, 97% yield) as the desired product. FTIR (KBr matrix), ν_{\max} (cm^{-1}): 3090 (w), 2978 (w), 2935 (w), 2915 (w), 2844 (w), 1638 (m), 1607 (vs, C=N), 1492 (w), 1433 (w), 1391 (w), 1362 (w), 1332 (w), 1307 (w), 1266 (m), 1173 (s), 1117 (s), 1085 (w), 1070 (m), 1055 (w), 1030 (s), 1004 (s), 967 (m), 910 (w), 896 (m), 881 (m), 857 (m), 793 (s), 761 (m), 742 (s), 688 (w), 617 (s), 542 (m), 415 (s). Anal. Calcd for $\text{C}_{29}\text{H}_{54}\text{N}_6\text{Cl}_2\text{Fe}\cdot\text{H}_2\text{O}$: C, 55.15; H, 8.94; N, 13.31. Found: C, 55.18; H, 8.82; N, 13.09.

[Fe(LN₄)NO], {FeNO}⁷, (1). To a 5 mL MeCN solution containing 1.7022 g (2.7744 mmol) of (Et₄N)₂[Fe(LN₄)Cl₂] was purged a stream of purified NO(g) for 2 min at RT under dark conditions. Addition of NO(g) resulted in an immediate dark green solution color (from orange-red) and eventual precipitation of a dark-green microcrystalline solid upon further

purging. The reaction mixture was then stirred for 30 min at RT under an atmosphere of NO in the headspace of the flask. After this time, excess NO(g) was removed by pulling vacuum and refilling with N₂. This solution was placed in a -20 °C refrigerator for 1 h to precipitate more product. The microcrystalline solid was filtered, washed with 3 mL of cold MeCN, and dried under vacuum to afford 0.680 g (2.18 mmol, 79%) of product. Green-colored X-ray quality crystals of **1** were grown by slow diffusion of pentane into a toluene solution of the complex at -20 °C. FTIR (KBr matrix), ν_{max} (cm⁻¹): 2928 (w), 1704 (vs, NO), 1654 (w), 1597 (s), 1578 (s), 1522 (w), 1509 (w), 1435 (m), 1396 (w), 1390 (w), 1367 (w), 1334 (w), 1310 (w), 1265 (w), 1252 (w), 1236 (w), 1196 (w), 1161 (w), 1136 (w), 1118 (w), 1084 (w), 1039 (m), 1014 (w), 984 (w), 964 (w), 922 (w), 895 (w), 884 (w), 855 (w), 781 (w), 768 (w), 744 (m), 733 (s), 679 (w), 607 (s), 567 (w), 474 (m), 447 (w), 416 (w). ν_{NO} (solution-state, CaF₂ windows, 0.1 mm spacers, RT): 1708 (MeCN); 1709 (2-MeTHF); 1709 (toluene). UV-vis (MeCN, 298 K), λ_{max} , nm (ϵ , M⁻¹ cm⁻¹): 330 (20,500), 661 (640), 720 (sh, 510). μ_{eff} (solid-state, 299 K): 1.68 μ_{B} ; μ_{eff} (solution-state, 298 K): 1.88 μ_{B} in CD₂Cl₂. Anal. Calcd for C₁₃H₁₄N₅OFe: C, 50.02; H, 4.52; N, 22.44. Found: C, 49.92; H, 4.19; N, 22.44.

[Fe(LN₄)(¹⁵NO)], {Fe¹⁵NO}⁷, (1-¹⁵NO). The isotopically-labeled complex **1**-¹⁵NO was prepared analogously to **1** except for using 0.9017 g (1.470 mmol) of (Et₄N)₂[Fe(LN₄)Cl₂] and ¹⁵NO(g). Yield: 0.3450 g (1.102 mmol, 75%). FTIR, ν_{NO} (cm⁻¹): 1673 (KBr matrix, $\Delta\nu_{\text{NO}}$: 31 cm⁻¹); 1676 (MeCN, $\Delta\nu_{\text{NO}}$: 32 cm⁻¹); 1678 (2-MeTHF, $\Delta\nu_{\text{NO}}$: 31 cm⁻¹); 1677 (toluene, $\Delta\nu_{\text{NO}}$: 32 cm⁻¹).

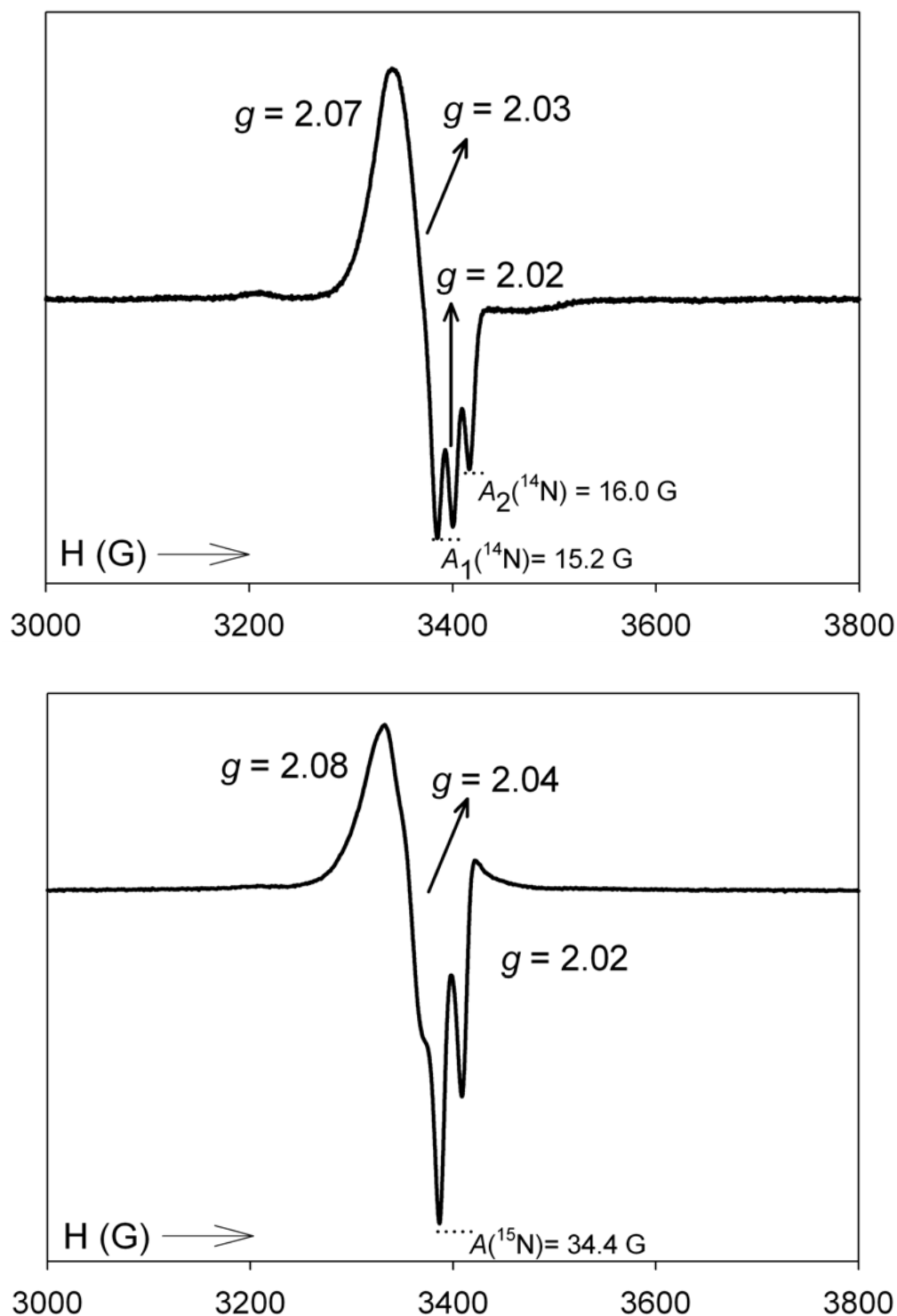


Figure S1. X-band EPR spectrum of $[\text{Fe}(\text{LN}_4)(\text{NO})]$ (**1**) (top) and $[\text{Fe}(\text{LN}_4)(^{15}\text{NO})]$ (**1- ^{15}NO**) (bottom) in toluene glass measured at 10 K. Selected g -values and $^{14}\text{N}/^{15}\text{N}$ hyperfine coupling constants are indicated. Spectrometer settings: microwave frequency, 9.60 GHz; microwave power, 0.5 mW (top), 2.02×10^{-4} mW (bottom); modulation frequency, 100 kHz; modulation amplitude, 6.48 G.

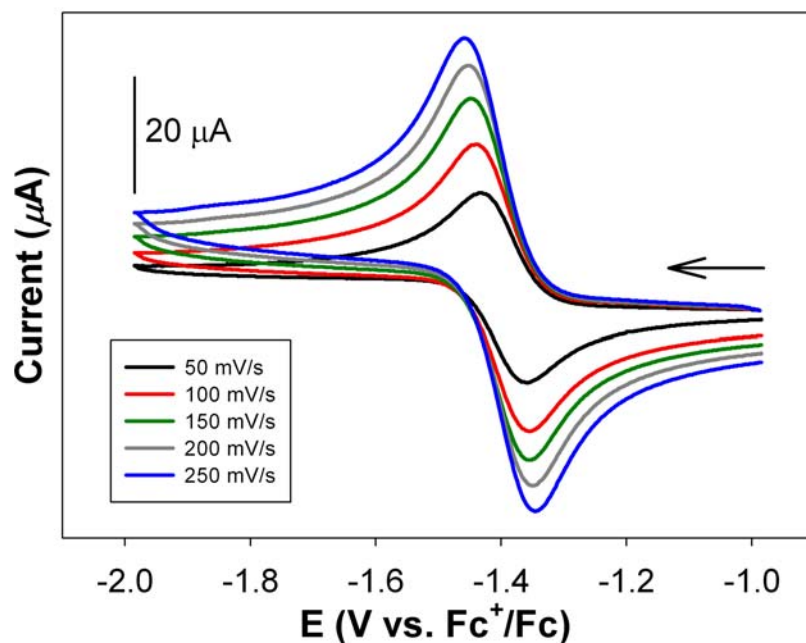


Figure S2. Cyclic voltammograms of a 2 mM MeCN solution of [Fe(LN₄)(NO)] (**1**) at different scan rates as indicated in the inset (0.1 M ⁿBu₄NPF₆ supporting electrolyte, glassy carbon working electrode, Pt-wire counter electrode, RT). Arrow displays direction of scan.

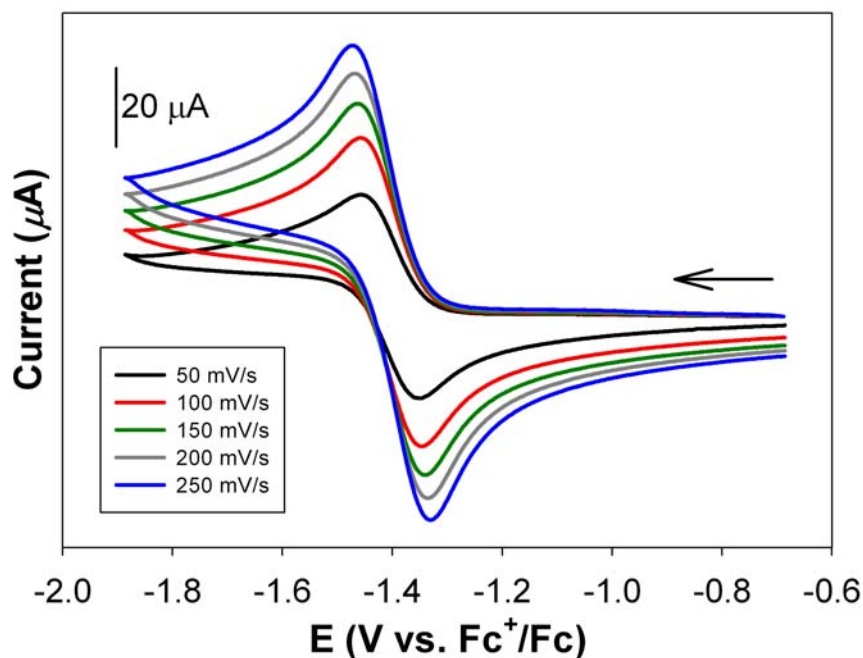


Figure S3. Cyclic voltammograms of a 4 mM MeCN solution of [Co(LN₄)(NO)] (**2**) at different scan rates as indicated in the inset (0.1 M ⁿBu₄NPF₆ supporting electrolyte, glassy carbon working electrode, Pt-wire counter electrode, RT). Arrow displays direction of scan.

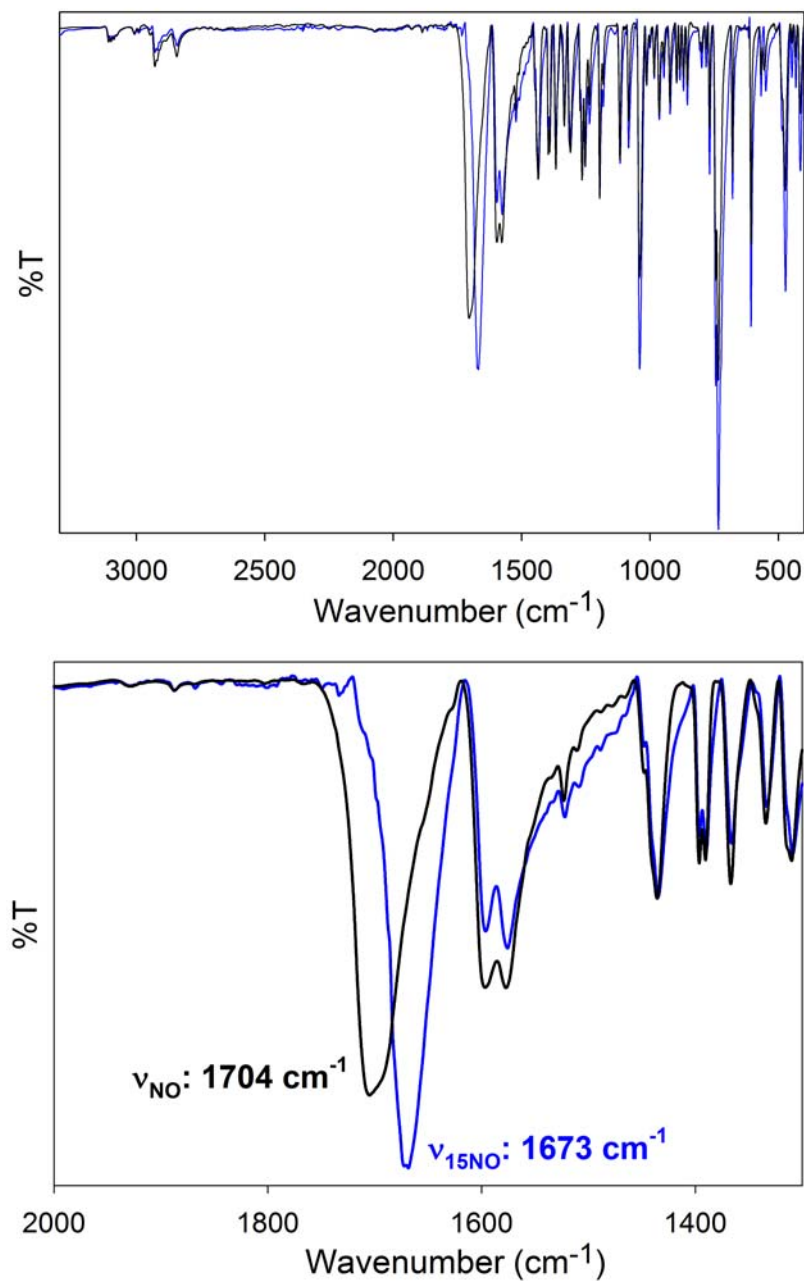


Figure S4. FTIR spectra of [Fe(LN₄)(NO)] (black line) (**1**) and [Fe(LN₄)(¹⁵NO)] (blue line) (**1-¹⁵NO**) in a KBr matrix. (*Top*) full FTIR spectrum; (*Bottom*) NO stretching frequency region.

[Co(LN₄)(NO)], {CoNO}⁸, (2). To a batch of LN₄ (0.1069 g, 0.4683 mmol) dispersed in 3 mL of dry MeCN was added a 2 mL MeCN slurry of NaH (0.0224 g, 0.9333 mmol), which resulted in H₂(g) evolution and the light purple solution color of the deprotonated ligand. To ensure complete deprotonation, an occasional vacuum was applied while stirring the solution further for ~15 min. To this solution was then added a 5 mL MeCN solution of (Et₄N)₂[CoCl₄] (0.2119 g, 0.4594 mmol) resulting in formation of a white precipitate (NaCl) and a green-red solution. The reaction mixture was stirred for another 1 h at 40 °C, which resulted in no further change. Finally, the solution was filtered to remove NaCl to obtain a clear green-red filtrate, which was concentrated to ~5 mL. To the filtrate was then purged a stream of purified NO(g) for 1.5 min at RT under dark conditions resulting in a gradual solution color change to dark red-brown upon NO(g) introduction. The resulting homogeneous solution was then stirred for 30 min at RT under an atmosphere of NO in the headspace of the flask. After this time, excess NO(g) was removed by pulling vacuum and refilling with N₂ and the solution was brought into the glovebox. Next, the solvent was stripped to dryness, ~10 mL of THF was added resulting in a dark-red solution with some pale precipitate (Et₄NCl). The THF solution was filtered and stripped to dryness to afford 0.1083 g (0.3436 mmol, 75%) of a dark colored microcrystalline product. Red X-ray quality crystals of **2** were grown by slow diffusion of Et₂O into a THF solution of the complex at -20 °C. FTIR (KBr matrix), ν_{max} (cm⁻¹): 3086 (w), 2922 (w), 2901 (w), 2846 (w), 1645 (vs, NO), 1595 (s), 1577 (s), 1439 (m), 1394 (m), 1364 (m), 1333 (m), 1317 (m), 1309 (m), 1273 (w), 1251 (m), 1234 (w), 1192 (w), 1180 (w), 1115 (m), 1099 (w), 1082 (m), 1035 (s), 954 (w), 929 (w), 898 (w), 880 (w), 858 (w), 804 (w), 771 (m), 740 (s), 725 (s), 678 (w), 609 (m), 571 (w), 544 (w), 481 (m), 440 (w), 422 (w). ν_{NO} (solution-state, CaF₂ window, 0.1 mm spacers, RT): 1665 (MeCN); 1662 (THF); 1666 (CH₂Cl₂). UV-vis (MeCN, 298

K), λ_{\max} , nm (ϵ , M⁻¹ cm⁻¹): 298 (12,700); 363 (sh 6,200); 520 (sh, 630). E_{1/2} (vs. Fc/Fc⁺, MeCN, RT): -1.40 V. ¹H NMR (500 MHz, THF-*d*₈, δ from protio solvent): 7.66 (s, 1H, CH=N), 7.30 (s, 1H, Ar-H), 6.71 (d, 1H, Ar-H), 6.14 (t, 1H, Ar-H), 3.37 (m, 4H, CH=N-CH₂), 1.93 (m, 1H, CH₂-C(H)(H)-CH₂), 1.58 (m, 1H, CH₂-C(H)(H)-CH₂). Anal. Calcd for C₁₃H₁₄N₅OCo: C, 49.53; H, 4.48; N, 22.22. Found: C, 49.73; H, 4.47; N, 21.67. Compound may contain residual THF resulting in the lower than expected percent N.

[Co(LN₄)(¹⁵NO)], {Co¹⁵NO}⁸, (2-¹⁵NO). The isotopically-labeled complex 2-¹⁵NO was prepared analogously to **2** except for using 0.2028 g (0.4397 mmol) of (Et₄N)₂[CoCl₄], 0.1003 g (0.4394 mmol) of LN₄, and 0.0214 g (0.8917 mmol) of NaH to generate (Et₄N)₂[Co(LN₄)Cl₂] *in situ* followed by purging ¹⁵NO(g). Yield: 0.070 g (0.221 mmol, 50%). FTIR, ν_{NO} (cm⁻¹): 1617 (KBr matrix, $\Delta\nu_{\text{NO}}$: 28 cm⁻¹); 1636 (MeCN, $\Delta\nu_{\text{NO}}$: 29 cm⁻¹); 1633 (THF, $\Delta\nu_{\text{NO}}$: 29 cm⁻¹); 1639 (CH₂Cl₂, $\Delta\nu_{\text{NO}}$: 27 cm⁻¹). ¹⁵N NMR (50.7 MHz, THF-*d*₈, δ from CH₃NO₂): 821.

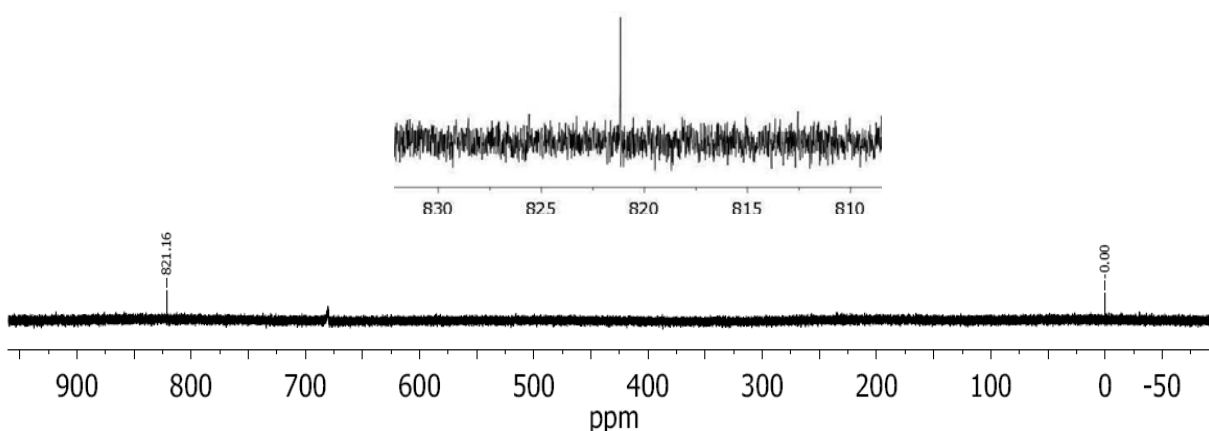


Figure S5. ¹⁵N NMR spectrum of [Co(LN₄)(¹⁵NO)] (2-¹⁵NO) in THF-*d*₈ at 298 K (CH₃NO₂ used as external standard). Inset: expansion of the ¹⁵N = 821 ppm peak of the NO ligand.

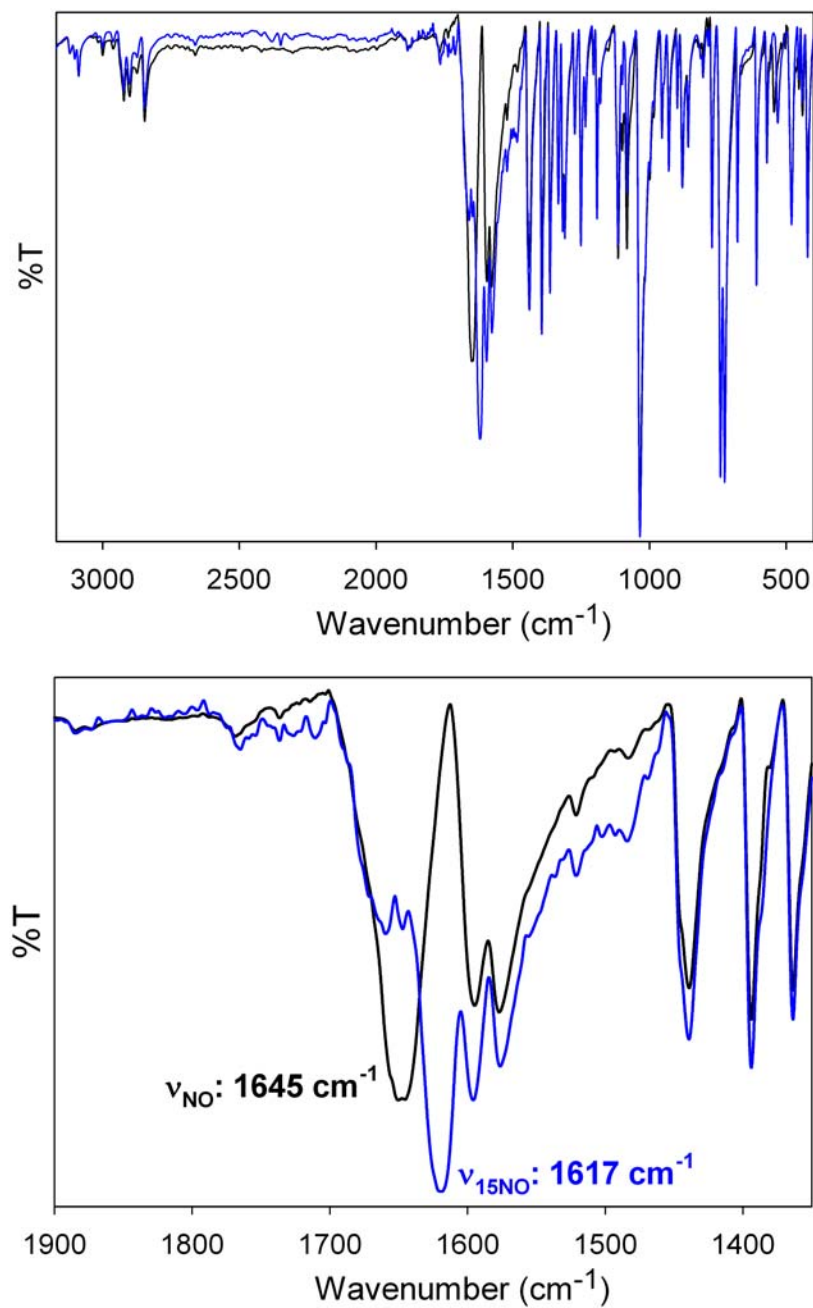


Figure S6. FTIR spectra of [Co(LN₄)(NO)] (black line) (**2**) and [Co(LN₄)(¹⁵NO)] (blue line) (**2-¹⁵NO**) in a KBr matrix. (*Top*) full FTIR spectrum; (*Bottom*) NO stretching frequency region.

[Co(Cp*)₂][Fe(LN₄)(NO)], {FeNO}⁸, (3**).** To a 10 mL toluene/THF solvent mixture (1:1 v/v) of **1** (0.1530 g, 0.4902 mmol) was added a 10 mL toluene solution of [Co(Cp*)₂] (0.1615 g, 0.4903 mmol) at RT. The solution color changed immediately from green to dark purple with precipitation of a dark colored solid within 15 min. This solution was allowed to stir further for 1 h at RT during which time no further changes were observed. The precipitate was filtered, washed with cold toluene (3×2 mL), followed by pentane (3×5 mL), and dried under vacuum to yield 0.3010 g (0.4692 mmol, 96%) of dark colored product. FTIR (KBr matrix), ν_{\max} (cm⁻¹): 3084 (m), 2911 (m), 2838 (m), 1656 (w), 1604 (vs, NO), 1590 (s), 1503 (m), 1477 (s), 1434 (m), 1389 (m), 1369 (m), 1334 (m), 1310 (m), 1266 (m), 1221 (w), 1191 (w), 1174 (w), 1118 (m), 1072 (m), 1029 (s), 968 (w), 913 (w), 895 (m), 858 (w), 768 (w), 735 (s), 697 (m), 616 (m), 564 (m), 468 (w), 445 (m). UV-vis (MeCN, 298 K), λ_{\max} , nm, (ϵ , M⁻¹ cm⁻¹): 293 (52,800), 560 (1800), 781 (450). HRMS-API (m/z): calcd for C₁₃H₁₄N₅OFe (anion of **3**), 312.0553; found, 312.0553. ¹H NMR (500 MHz, CD₃CN, δ from protio solvent): 7.96 (s, 1H, CH=N), 7.79 (s, 1H, CH=N), 6.76 (d, 1H, ArH), 6.65 (s, 1H, ArH), 6.58 (m, 1H, ArH), 6.48 (s, 1H, ArH), 6.20 (s, 1H, ArH), 6.06 (m, 1H, ArH), 3.79 (s, 2H, CH=N-CH₂), 3.17 (t, 2H, CH=N-CH₂), 1.82 (p, 1H, N-CH₂-CH₂-CH₂-N), 1.54 (p, 1H, N-CH₂-CH₂-CH₂-N), 1.65 (s, 30H, Cp^{*}-CH₃). Anal. Calcd for C₃₃H₄₄N₅OFe: C, 61.78; H, 6.91; N, 10.92. Found: C, 61.67; H, 6.82; N, 10.86.

[Co(Cp*)₂][Fe(LN₄)(¹⁵NO)], {Fe-¹⁵NO}⁸, (3**-¹⁵NO).** The isotopically-labeled complex **3**-¹⁵NO was prepared analogously to **3** except for using 0.0788 g (0.2517 mmol) of **1**-¹⁵NO. Yield: 0.1360 g (0.2118 mmol, 84%). FTIR, ν_{NO} (cm⁻¹): 1570 cm⁻¹ (KBr matrix, $\Delta\nu_{\text{NO}}$: 34 cm⁻¹). HRMS-API (m/z): calcd for C₁₃H₁₄N₄O¹⁵NFe (anion of **3**-¹⁵NO), 313.0519; found, 313.0521. ¹⁵N NMR (50.7 MHz, CD₃CN, δ from CH₃NO₂): 743.

Oxidation of $[\text{Co}(\text{Cp}^*)_2][\text{Fe}(\text{LN}_4)(\text{NO})]$ (3**) with FcPF_6 to establish the $\{\text{FeNO}\}^8 \leftrightarrow \{\text{FeNO}\}^7$ interconversion.** To a 2 mL MeCN solution of **3** (0.0334 g, 0.0521 mmol) was added a 2 mL MeCN solution of FcPF_6 (0.0179 g, 0.0541 mmol) at RT. The color immediately changed from red to a brownish green which became greener while stirring over 0.5 h. The reaction mixture was stirred further for 2 h at RT during which time no further changes were observed. The reaction mixture was filtered to remove any insolubles, the solvent was evaporated from the green filtrate, and the residue was washed with cold Et_2O (3×5 mL) and dried to obtain 0.0138 g (0.0442 mmol, 85%) of the oxidized $\{\text{FeNO}\}^7$ product **1**. The spectra match that of **1** and confirm the formation of $[\text{Fe}(\text{LN}_4)(\text{NO})]$ (**1**) as the one-electron oxidized product from the reaction of **3** with FcPF_6 .

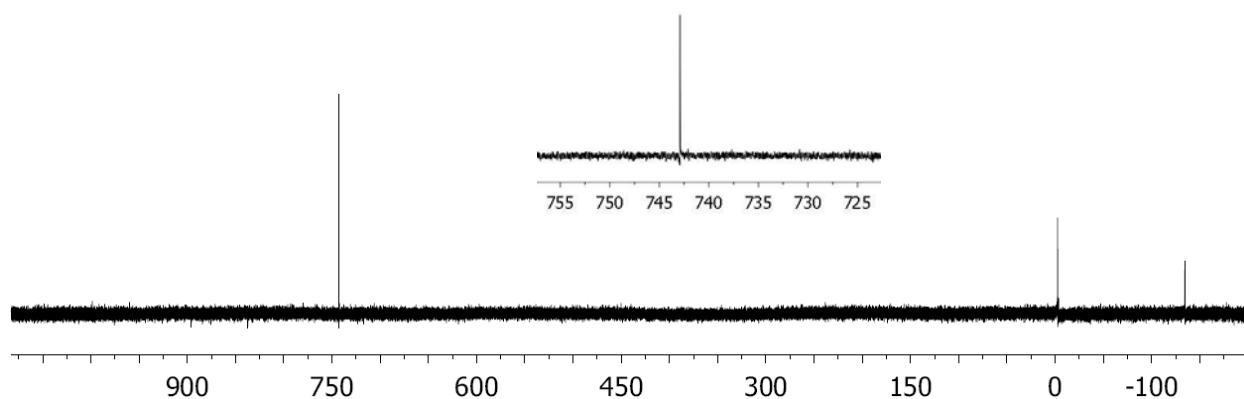


Figure S7. ^{15}N NMR spectrum of $[\text{Co}(\text{Cp}^*)_2][\text{Fe}(\text{LN}_4)(^{15}\text{NO})]$ (**3- ^{15}NO**) in CD_3CN at 298 K. Peak at -135 ppm is tentatively assigned to a coordinated CH_3CN ligand³ (CH_3NO_2 used as external standard). Inset: expansion of the $^{15}\text{N} = 743$ ppm peak of the NO ligand.

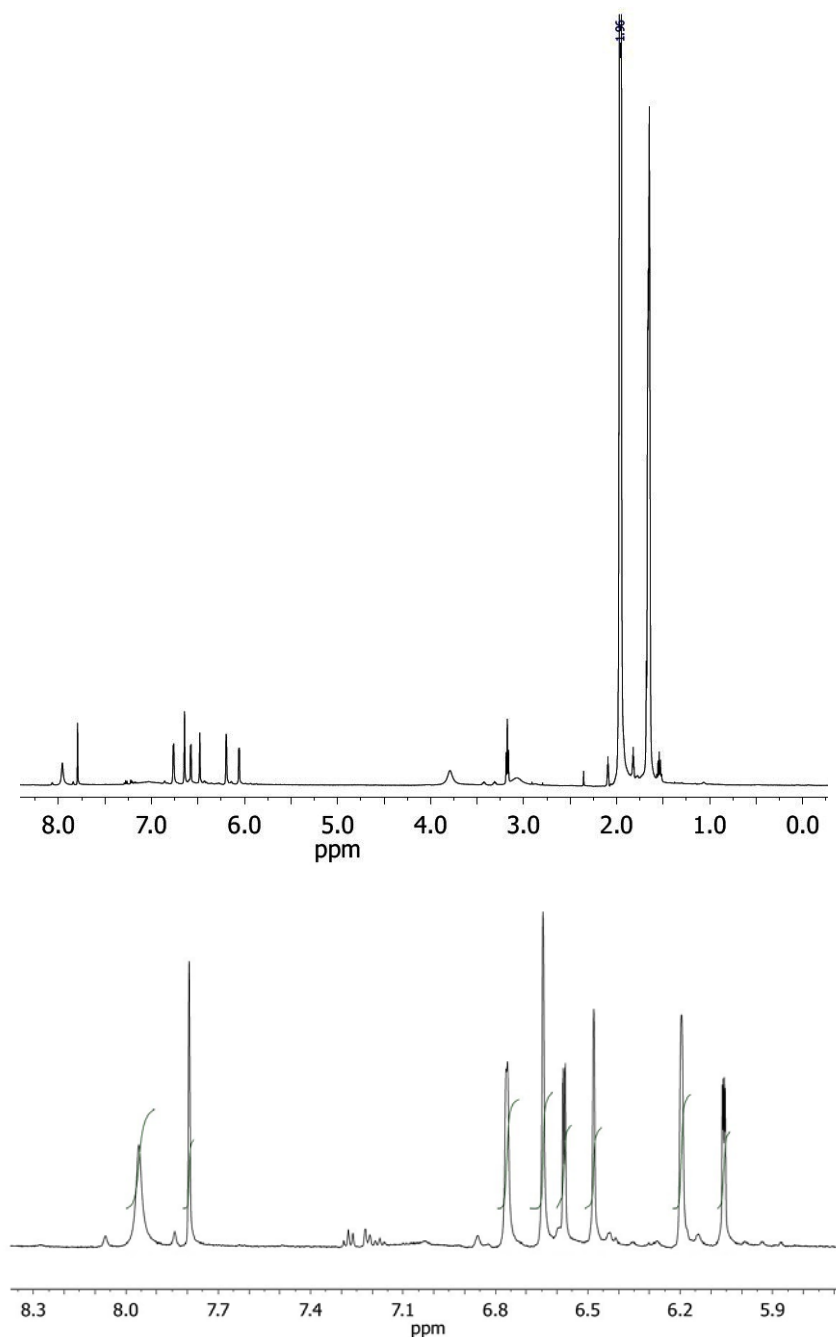


Figure S8. Complete (top) and aromatic region (bottom) of the ¹H NMR spectrum of [Co(Cp*)₂][Fe(LN₄)(NO)] (**3**) in CD₃CN at 298 K. Peaks at 1.98 and 2.11 are from residual CH₃CN and H₂O, respectively. The peak at 1.65 is from the CH₃-Cp groups of the [Co(Cp*)₂]⁺ counter-cation. Small peaks due to residual toluene from the synthetic workup are also observed at 2.33 and 7.15-7.30 ppm.

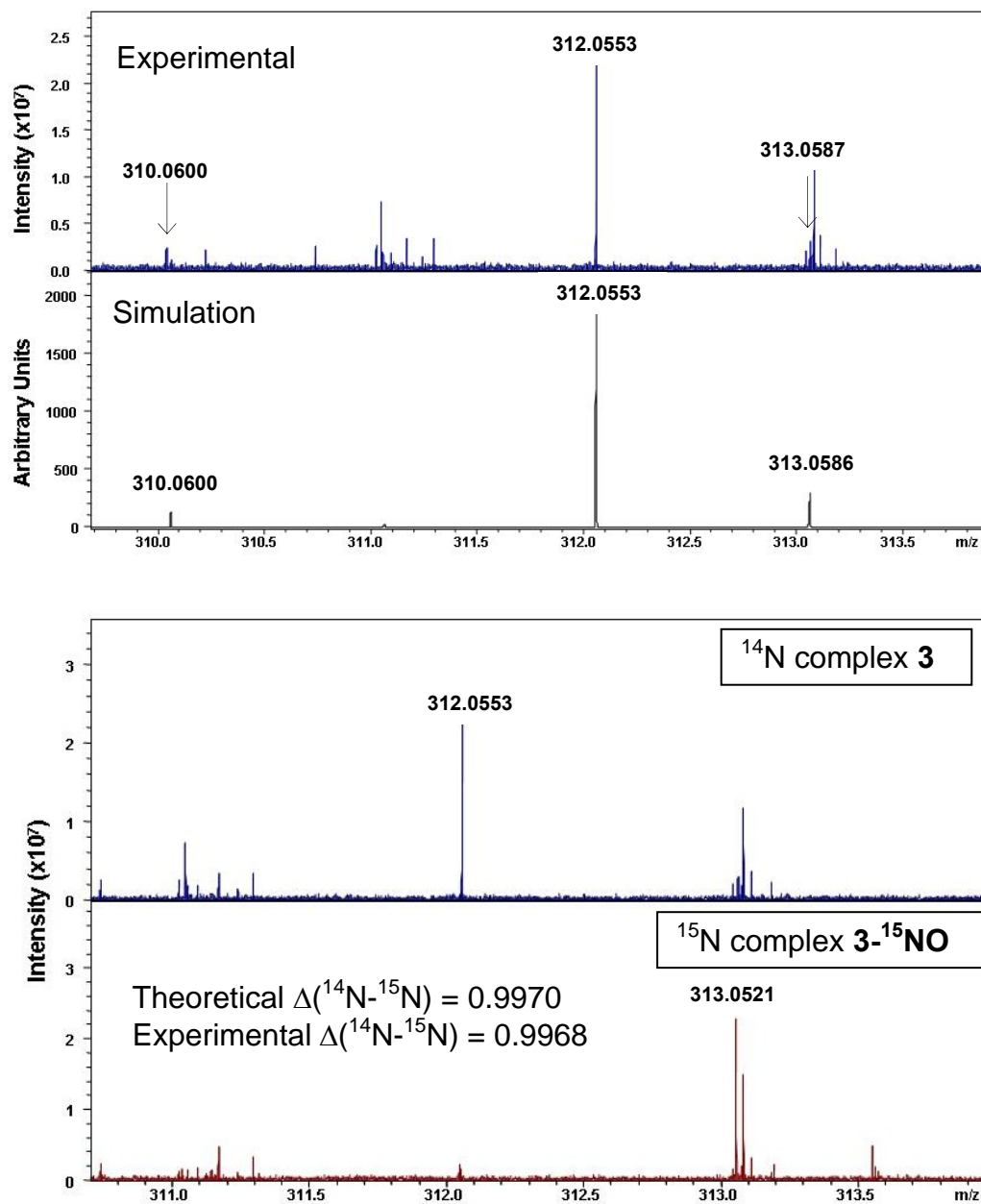


Figure S9. (Top) High resolution FT-ICR-MS of an MeCN solution of $[\text{Co}(\text{Cp}^*)_2][\text{Fe}(\text{LN}_4)(\text{NO})]$ (**3**) in negative-ion mode along with simulated MS. (Bottom) Overlay of the FT-ICR-MS of **3** and ^{15}N isotope **3- ^{15}N NO**.

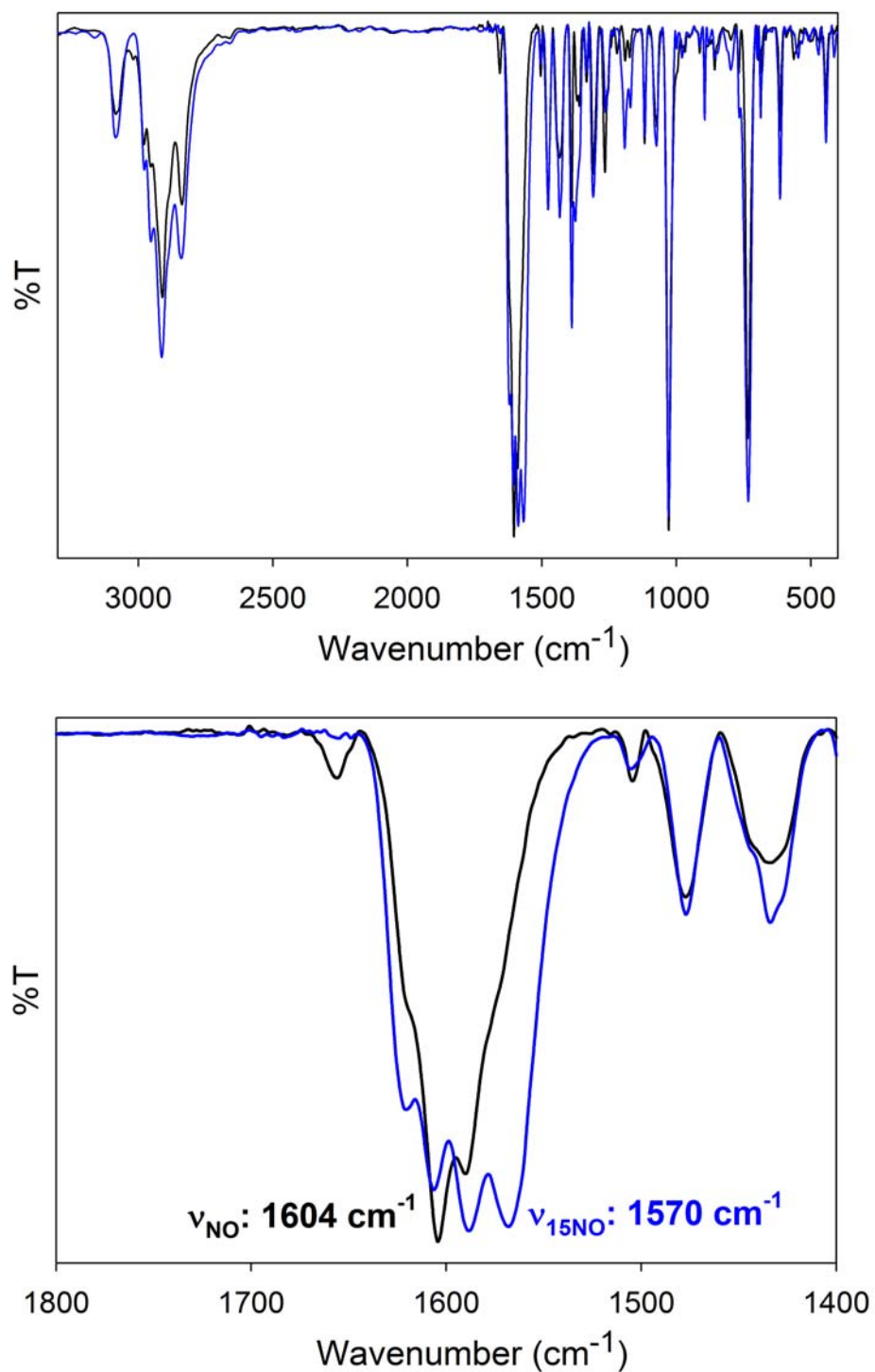


Figure S10. FTIR spectra of $[\text{Co}(\text{Cp}^*)_2][\text{Fe}(\text{LN}_4)(\text{NO})]$ (black line) (**3**) and $[\text{Co}(\text{Cp}^*)_2][\text{Fe}(\text{LN}_4)(^{15}\text{NO})]$ (blue line) (**3- ^{15}NO**) in a KBr matrix. (*Top*) full FTIR spectrum; (*Bottom*) NO stretching frequency region.

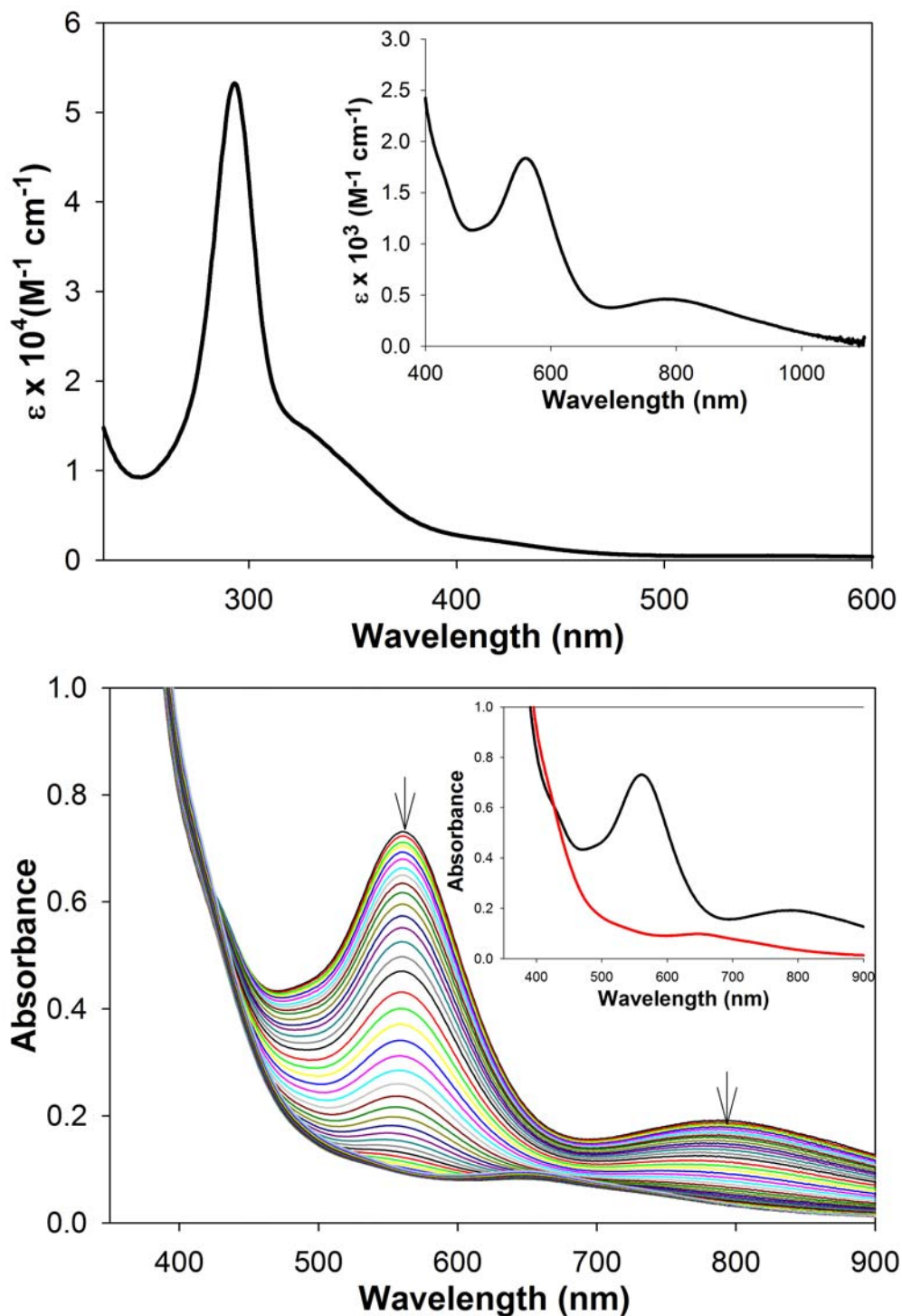


Figure S11. (Top) UV-vis spectrum of a 0.023 mM MeCN solution of **3** at 298 K. Inset shows an expansion of the visible region of a more concentrated MeCN solution of **3** (0.33 mM, 298 K). (Bottom) UV-vis spectral decay of a 0.42 mM MeCN solution of **3** at 298 K (each trace recorded at 15 min intervals, 13 h total time). Inset shows the initial (black) and final (red) spectrum of **3**.

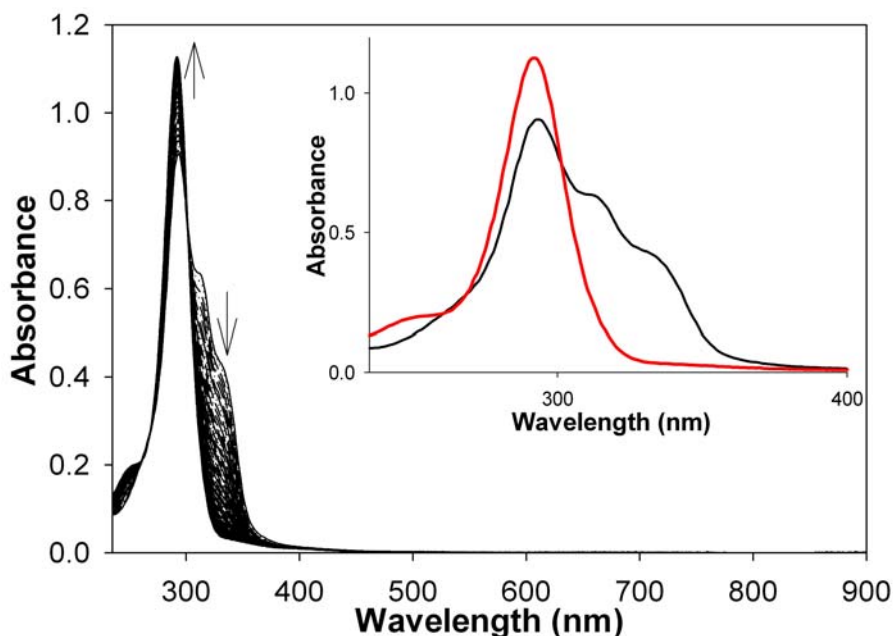


Figure S12. UV-vis spectral decay of a 0.012 mM solution of **3** in pH 7.2 phosphate buffered saline at 293 K. Arrows indicate direction of change (each trace recorded at 1 min intervals, 1.5 h total time, $t_{1/2}$ = 15 min). Inset: Expansion showing the initial (black trace) and final (red trace, 90 min scan) spectrum of **3**. Due to the low solubility of **3** in aqueous solution the visible bands were not observed. Spectrum was recorded by adding a 10 μ L MeCN aliquot of **3** dissolved (stock concentration: 3.5 mM) to 3.0 mL of buffer in a UV-vis cuvette.

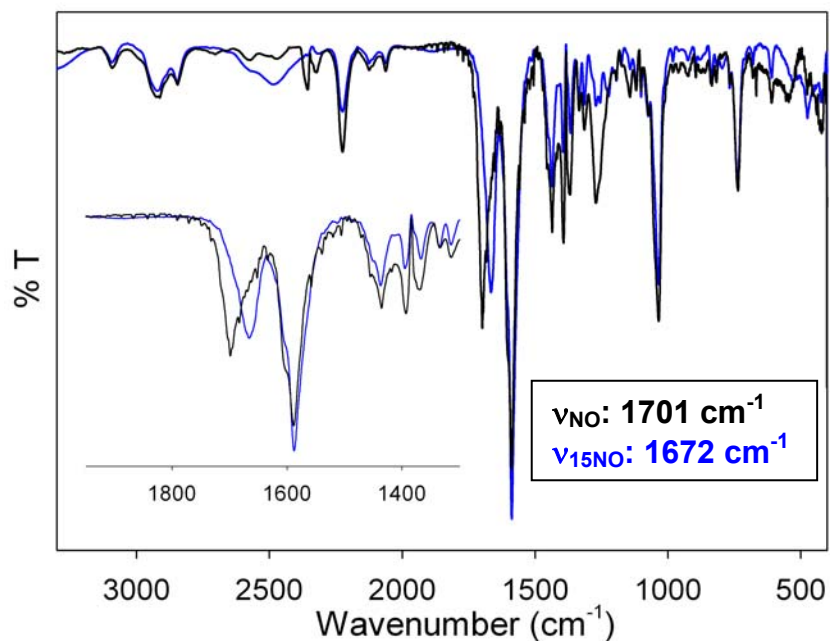


Figure S13. FTIR spectra of products formed after allowing complex **3** to stir in acetone for 12 h at RT. Selected IR bands are labeled (products from **3** shown in black and products from **3**-¹⁵NO shown in blue).

Reactivity

Reaction with metmyoglobin (metMb) and ferrous myoglobin (deoxyMb). All manipulations of Mb (from equine skeletal muscle) were monitored by electronic absorption spectroscopy under anaerobic conditions in 50 mM phosphate buffer or phosphate buffered saline as noted (pH 7.2) at 293 K. The reductive nitrosylation from the reduced nitrogen oxide ligands of the {MNO}⁸ complexes **2** and **3** to metMb were performed with freshly prepared solutions in MeCN on the day of the experiment due to the slow disproportionation of **3** in solution. In general, small MeCN aliquots of the MNO species (10-20 μ L) were added to a UV-vis cuvette containing 3.0-3.1 mL of metMb or deoxyMb in buffer. The UV-vis spectra were immediately monitored after addition of the complexes to the UV-vis cell containing metMb. No reaction was observed with metMb and the {FeNO}⁷ complex **1** under identical conditions and the same time period. Complex **1**, however, does appear to form MbNO over a long (1 h) time period (data not shown).

metMb + [Co(LN₄)(NO)] (2**).** A 9 μ L MeCN aliquot of **2** (5.0 mM, 5.6 mol-equiv) was added via gas-tight microsyringe to a quartz UV-vis cell containing metMb (2.72 μ M, 3.0 mL total volume) in phosphate buffer (pH 7.2) through the septum in the cell cap and the UV-vis spectrum was recorded immediately. No immediate change resulted indicating no formation of the MbNO adduct (Soret band of metMb, λ_{max} : 409 nm, ϵ : 188 mM⁻¹ cm⁻¹ see Figure S14).⁴ No further change was observed over a time period of 10 h.

metMb + [Co(Cp*)₂][Fe(LN₄)(NO)] (3**).** A 9 μ L MeCN aliquot of **3** (5.0 mM, 5.0 mol-equiv) was added via gas-tight microsyringe to a quartz UV-vis cell containing metMb (2.97 μ M, 3.0 mL total volume) in phosphate buffer (pH 7.2) through the septum in the cell cap and the UV-vis spectrum was recorded immediately. An instantaneous red-shift of the metMb Soret band and the appearance of the double-humped Q-bands at ~550 nm confirmed the near

quantitative formation of MbNO (Soret band of MbNO, λ_{max} : 422 nm, ϵ : 147 mM⁻¹ cm⁻¹; A_{422} = 0.4064 corresponds to 2.76 μ M of MbNO formed (93% yield), see Figure S15).⁴

metMb + GSH + [Co(Cp*)₂][Fe(LN₄)(NO)] (3). A 4.48 μ M metMb solution in pH 7.2 phosphate buffer was prepared and its absorption spectrum recorded in a quartz UV-vis cell (3.1 mL total volume). To this metMb solution was added 25 mol-equiv of GSH resulting in no UV-vis spectral changes. To this metMb/GSH solution was then added a 14 μ L MeCN aliquot of **3** (5.0 mM, 5.0 mol-equiv) via gas-tight microsyringe to the cell through the septum cap and the UV-vis was recorded immediately. No immediate change resulted indicating no formation of the MbNO adduct (Soret band of metMb, λ_{max} : 409 nm, ϵ : 188 mM⁻¹ cm⁻¹ see Figure S16).⁴ No further change was observed over a time period of 1.5 h.

metMb + dithionite (=deoxyMb) + [Co(Cp*)₂][Fe(LN₄)(NO)] (3). A standard of ferrous myoglobin (deoxyMb) solution (3.1 mL total volume) was prepared by mixing 5 mol-equiv of sodium dithionite with metMb in pH 7.2 phosphate buffer, which resulted in a red-shift in the Soret band to 435 nm characteristic of deoxyMb (Soret band of deoxyMb, λ_{max} : 435 nm, ϵ : 122 mM⁻¹ cm⁻¹; A_{435} = 0.764 corresponding to 6.26 μ M of deoxyMb).⁴ To the deoxyMb solution was then added a 20 μ L MeCN aliquot of **3** (5.0 mM, 5.0 mol-equiv) via gas-tight microsyringe and the UV-vis spectrum was recorded immediately. An instantaneous blue-shift of the deoxyMb Soret band and the appearance of the double-humped Q-bands at ~550 nm confirmed the formation of MbNO (Soret band of MbNO, λ_{max} : 422 nm, ϵ : 147 mM⁻¹ cm⁻¹; A_{422} = 0.8941 corresponding to 6.08 μ M MbNO formation (97% yield), see Figure S17).⁴ No further change was observed over a time period of 1.5 h.

metMb + dithionite (=deoxyMb) + [Fe(LN₄)(NO)] (1). A standard of deoxyMb solution (3.1 mL total volume) was prepared by mixing 5 mol-equiv of sodium dithionite with

metMb in pH 7.2 phosphate buffer, which resulted in a red-shift in the Soret band to 435 nm characteristic of deoxyMb (Soret band of deoxyMb, λ_{max} : 435 nm, ϵ : 122 mM⁻¹ cm⁻¹; A_{435} = 0.674 corresponding to 5.52 μ M of deoxyMb).⁴ To the deoxyMb solution was then added an 18 μ L MeCN aliquot of **1** (5.0 mM, 5.0 mol-equiv) via gas-tight microsyringe and the UV-vis spectrum was recorded immediately. An instantaneous blue-shift of the deoxyMb Soret band and the appearance of the double-humped Q-bands at ~550 nm confirmed the formation of MbNO (Soret band of MbNO, λ_{max} : 422 nm, ϵ : 147 mM⁻¹ cm⁻¹; A_{422} = 0.7705 corresponds to near quantitative 5.24 μ M MbNO formation (95% yield), see Figure S18).⁴ No further change was observed over a time period of 1.5 h.

metMb + [Co(Cp*)₂][Fe(LN₄)(NO)] (3**) – stoichiometric additions.** A 3.72-3.90 μ M metMb solution (determined spectrophotometrically using the known ϵ = 188 mM⁻¹ cm⁻¹ for the Soret band at 409 nm)⁴ in pH 7.2 phosphate buffered saline was prepared and its absorption spectrum recorded in a quartz UV-vis cell (3.0 mL total volume). To this metMb solution was then added 10 μ L MeCN aliquots of the appropriate stock solutions of **3** (from 1-5 mol-equiv) via gas-tight microsyringe to the cell through the septum cap and the UV-vis recorded immediately. Spectra were collected at 1 min intervals for a total time of 10 min. All major changes occurred within 2 min, with only very minor changes in the Soret band observed after the 10 min run time. Changes in the UV-vis are depicted in figures S19-S20 and indicate that at least 3 mol-equiv of **3** are required for full reductive nitrosylation of metMb under the conditions employed (see Figure S21).

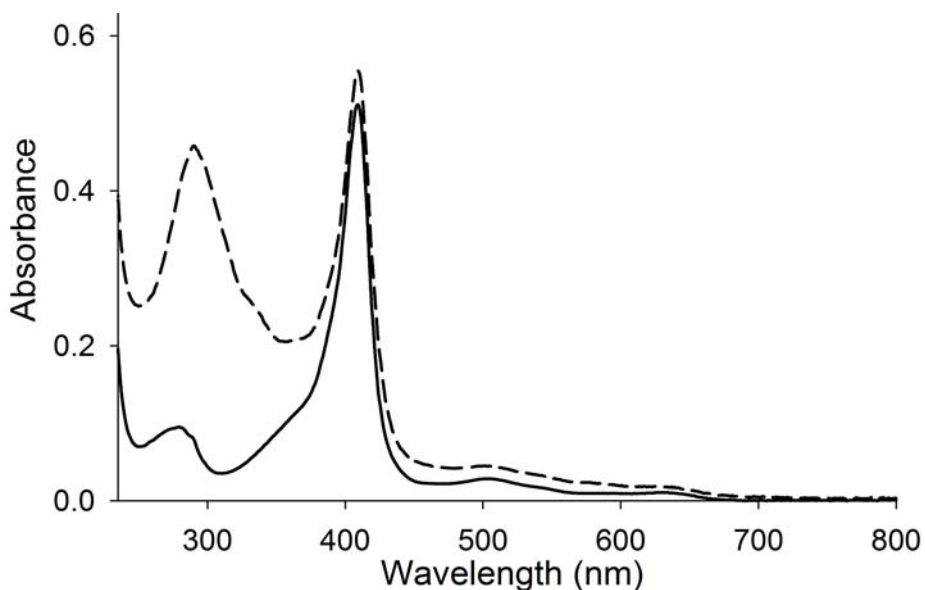


Figure S14. UV-vis spectra of a 2.72 μM solution of metMb before (black line) and after (1 h, black dashed line) addition of complex **2** (5 mol-equiv) at 293 K in 50 mM phosphate buffer (pH 7.2). Peak at $\lambda = 298$ nm in the dashed spectrum is due to ligand π -transitions of **2**. Slight increase in absorbance is presumably due to overlapping absorbance with **2**.

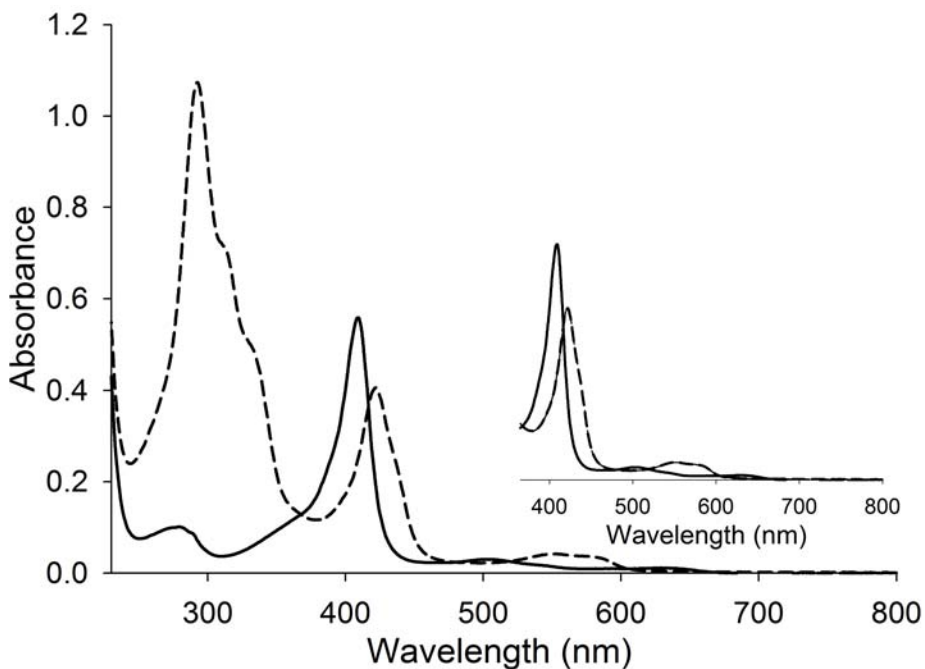


Figure S15. UV-vis spectra of a 2.97 μM solution of metMb before (black line) and immediately after (black dashed line) addition of complex **3** (5 mol-equiv) at 293 K in 50 mM phosphate buffer (pH 7.2). Dashed trace is indicative of the formation of Mb-NO. Inset: expansion of Mb absorption region. Peaks at $\lambda \sim 300$ nm in the dashed spectrum are due to ligand and $[\text{Co}(\text{Cp}^*)_2]^+$ π -transitions of **3**.

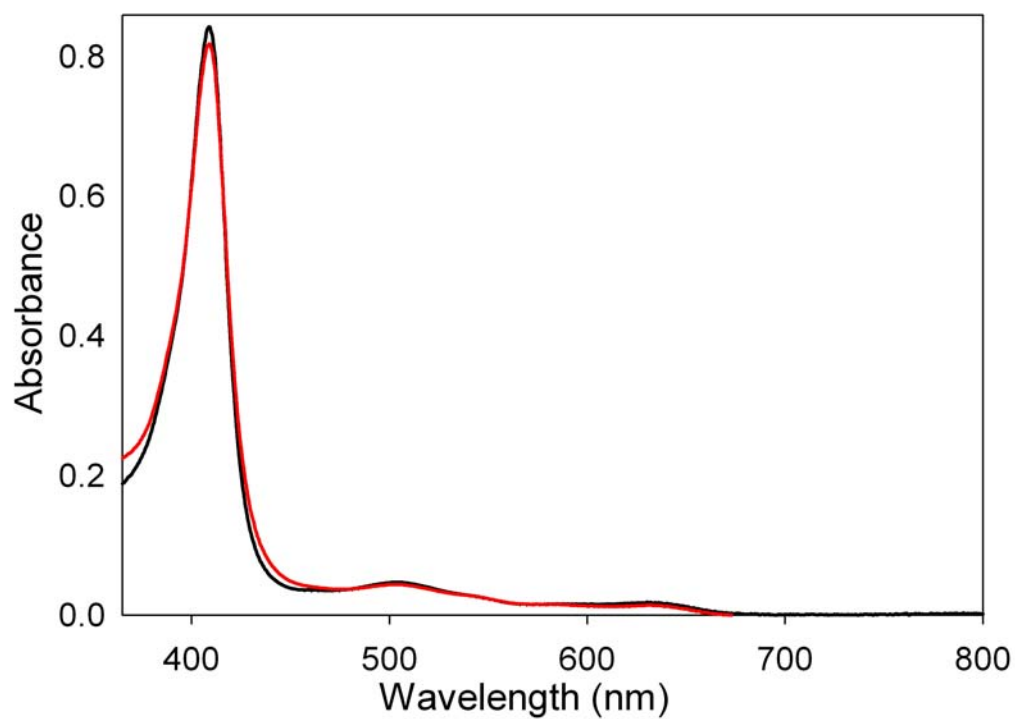


Figure S16. UV-vis spectra of a 4.48 μM solution of metMb containing 25 mol-equiv of GSH before (black trace) and after (red trace) 90 min mixing with complex **3** (5 mol-equiv) at 293 K in 50 mM phosphate buffer (pH 7.2). No reaction between **3** and metMb is observed with GSH present.

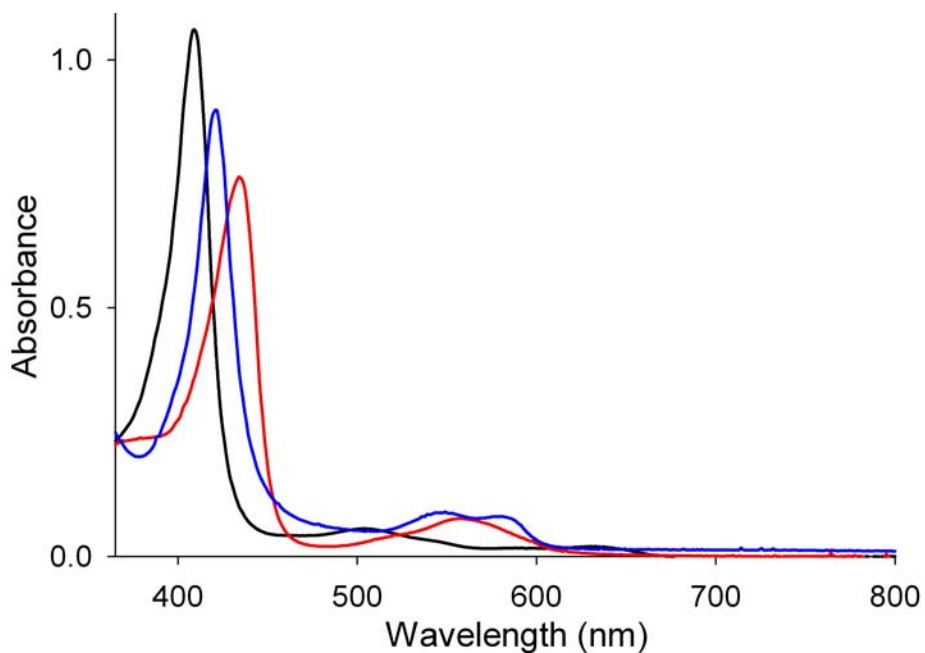


Figure S17. UV-vis spectra of metMb before (black trace), after addition of 5 mol-equiv of sodium dithionite to result in formation of deoxyMb (6.26 mM, red trace), and immediately after (blue trace) addition of complex **3** (5 mol-equiv) at 293 K in 50 mM phosphate buffer (pH 7.2).

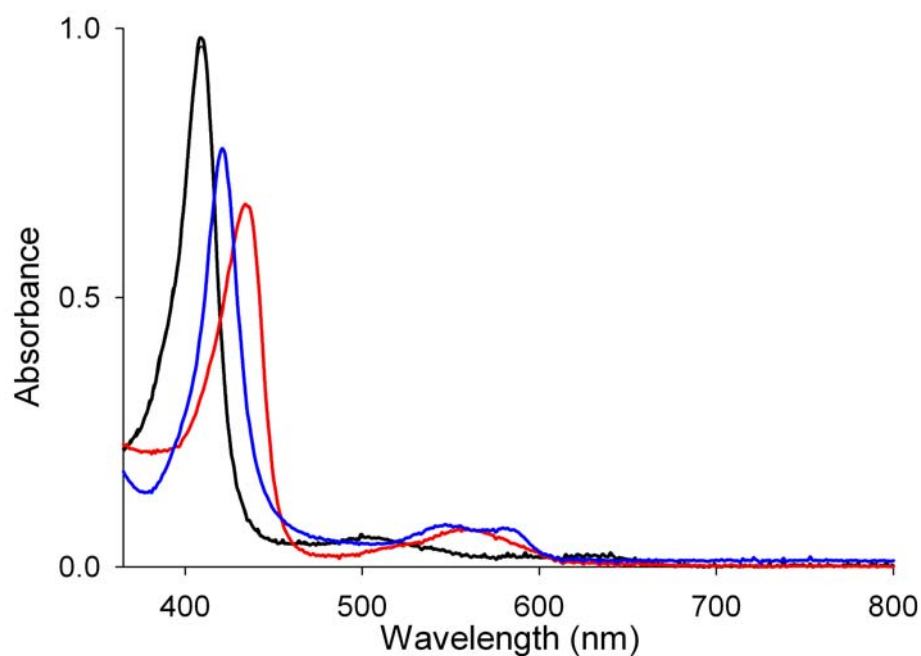


Figure S18. UV-vis spectra of metMb before (black trace), after addition of 5 mol-equiv of sodium dithionite to result in formation of deoxyMb (5.53 mM, red trace), and immediately after (blue trace) addition of complex **1** (5 mol-equiv) at 293 K in 50 mM phosphate buffer (pH 7.2).

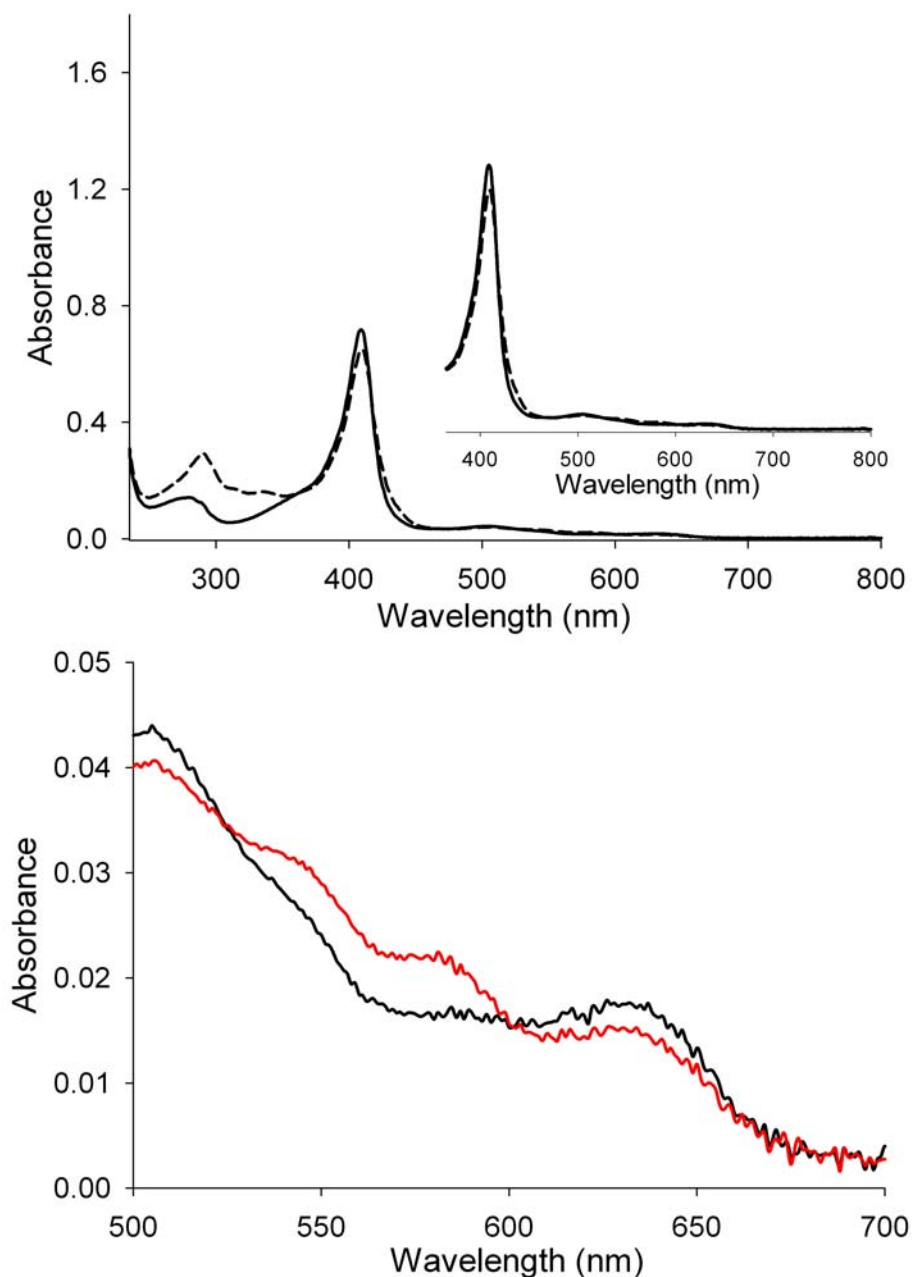


Figure S19. (*Top*) UV-vis spectra of a 3.90 μM solution of metMb before (black line) and immediately after (black dashed line) addition of complex **3** (1 mol-equiv) at 293 K in 50 mM phosphate buffered saline (pH 7.2). Inset: expansion of Mb Soret absorption region. Peaks at $\lambda \sim 300$ nm in the dashed spectrum are due to ligand and $[\text{Co}(\text{Cp}^*)_2]^+$ π -transitions of **3**. (*Bottom*) Expansion of Mb Q-band absorption region before (black trace) and after (red trace) addition of 1 mol-equiv of **3**.

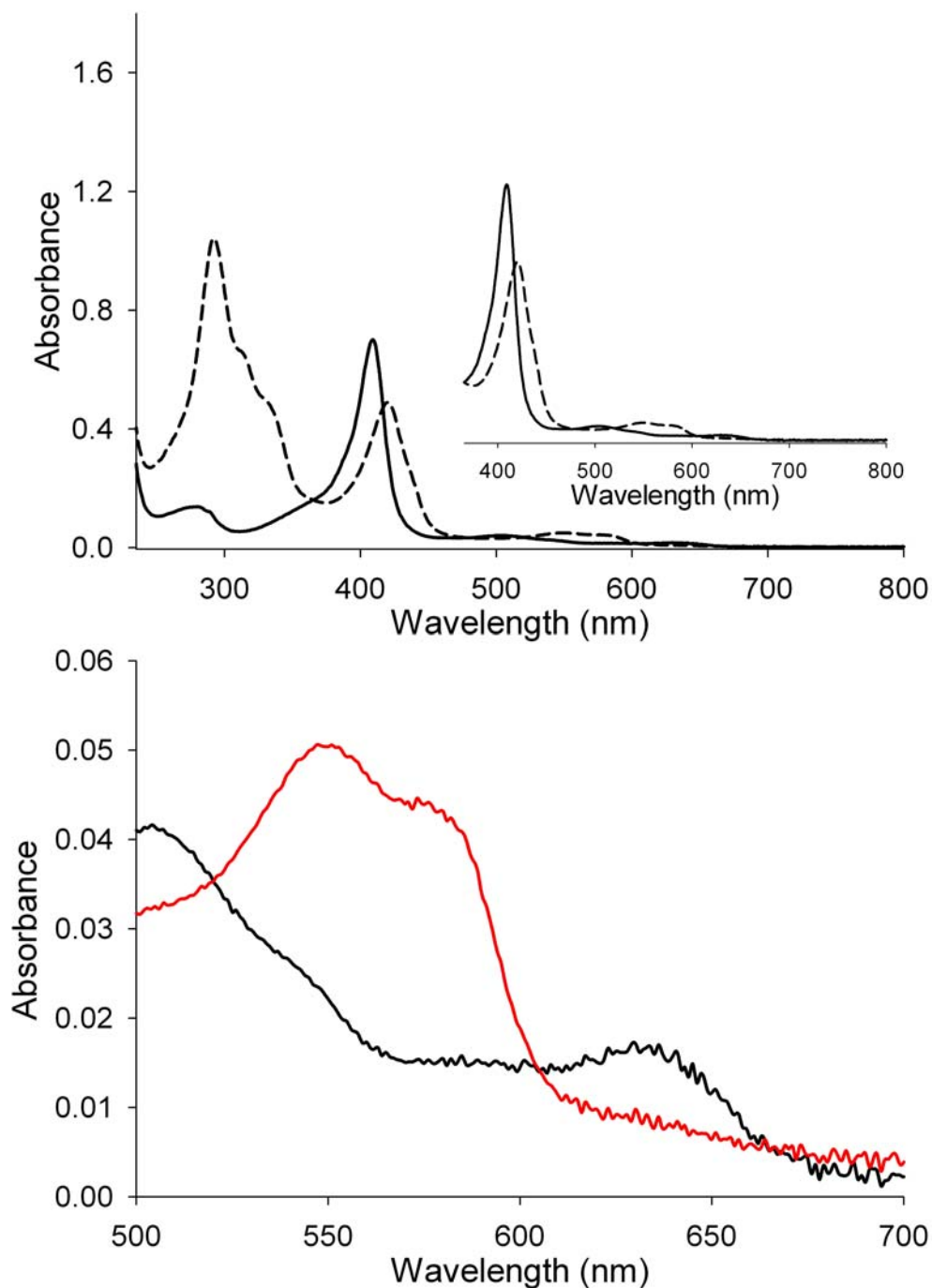


Figure S20. (*Top*) UV-vis spectra of a 3.90 μM solution of metMb before (black line) and immediately after (black dashed line) addition of complex **3** (**3 mol-equiv**) at 293 K in 50 mM phosphate buffered saline (pH 7.2). Inset: expansion of Mb Soret absorption region. Peaks at $\lambda \sim 300$ nm in the dashed spectrum are due to ligand and $[\text{Co}(\text{Cp}^*)_2]^+$ π -transitions of **3**. (*Bottom*) Expansion of Mb Q-band absorption region before (black trace) and after (red trace) addition of 3 mol-equiv of **3**.

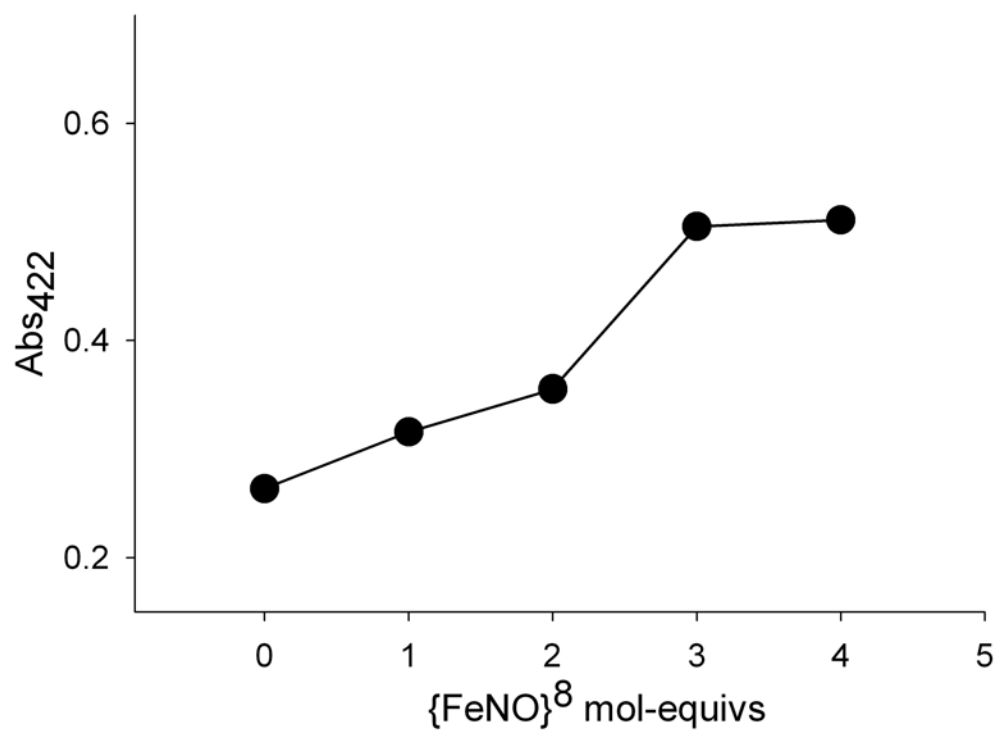


Figure S21. Plot of Abs₄₂₂ versus {FeNO}⁸ (**3**) mol-equivs (see experimental parameters above).

X-ray Crystallographic Data Collection and Structure Solution and Refinement. Dark-green crystals of $[\text{Fe}(\text{LN}_4)(\text{NO})]$ (**1**) and dark-red crystals of $[\text{Co}(\text{LN}_4)(\text{NO})]$ (**2**) were grown under anaerobic conditions by slow diffusion of pentane into a toluene solution of **1** and slow diffusion of Et_2O into a THF solution of **2** both at -20°C . Suitable crystals were mounted on a glass capillary. All geometric and intensity data were measured at 100 K on a Bruker SMART APEX II CCD X-ray diffractometer system equipped with graphite-monochromatic $\text{Mo K}\alpha$ radiation ($\lambda = 0.71073 \text{ \AA}$) with increasing ω (width 0.5° per frame) at a scan speed of 10 s/frame controlled by the SMART software package.⁵ The intensity data were corrected for Lorentz-polarization effects and for absorption⁶ and integrated with the SAINT software. Empirical absorption corrections were applied to structures using the SADABS program.⁷ The structures were solved by direct methods with refinement by full-matrix least-squares based on F^2 using the SHELXTL-97 software⁸ incorporated in the SHELXTL 6.1 software package.⁹ The hydrogen atoms were fixed in their calculated positions and refined using a riding model. All non-hydrogen atoms were refined anisotropically. Selected crystal data and metric parameters for complexes **1** and **2** are summarized in Table S1. Selected bond distances and angles for complexes **1** and **2** are given in Table S2. Perspective views of the complexes were obtained using ORTEP.¹⁰ ORTEP views of complexes **1** and **2** are illustrated in Figures S22-S23, respectively.

Table S1. Summary of crystal data and intensity collection and structure refinement parameters for [Fe(LN₄)(NO)] (**1**) and [Co(LN₄)(NO)] (**2**).

Parameters	1	2
Formula	C ₁₃ H ₁₄ FeN ₅ O	C ₁₃ H ₁₄ CoN ₅ O
Formula weight	312.14	315.22
Crystal system	Triclinic	Monoclinic
Space group	<i>P</i> -1	<i>P</i> 2 ₁ / <i>n</i>
Crystal color, habit	Green rectangle	red rectangle
<i>a</i> , Å	8.240(5)	10.445(5)
<i>b</i> , Å	9.982(5)	11.723(5)
<i>c</i> , Å	16.640(5)	11.030(5)
α , deg	82.977(5)	90.00
β , deg	83.088(5)	100.177(5)
γ , deg	73.325(5)	90.00
<i>V</i> , Å ³	1296.0(11)	1329.3(10)
<i>Z</i>	4	4
ρ_{calcd} , g/cm ⁻³	1.600	1.575
<i>T</i> , K	100(2)	100(2)
abs coeff, μ , mm ⁻¹	1.166	1.293
θ limits, deg	2.14-33.20	2.48-33.20
total no. of data	22511	22837
no. of unique data	9143	4896
no. of parameters	361	181
GOF on F ²	1.038	1.166
<i>R</i> ₁ , ^[a] %	2.93	2.43
<i>wR</i> ₂ , ^[b] %	7.86	7.56
max, min peaks, e/Å ³	0.785, -0.620	0.511, -0.941

$$^a R_1 = \sum |F_o| - |F_c| / \sum |F_o|; ^b wR_2 = \{\sum [w(F_o^2 - F_c^2)^2] / \sum [w(F_o^2)^2]\}^{1/2}.$$

Table S2. Selected bond distances (Å) and bond angles (deg) for [Fe(LN₄)(NO)] (**1**) and [Co(LN₄)(NO)] (**2**).

[Fe(LN ₄)(NO)] (1)				[Co(LN ₄)(NO)] (2)	
Molecule 1		Molecule 2			
Fe1- N1	1.9413(12)	Fe2- N6	1.9530(14)	Co1-N1	1.9277(10)
Fe1- N2	1.9730(11)	Fe2 -N7	1.9731(11)	Co1- N2	1.9433(11)
Fe1- N3	1.9939(12)	Fe2 -N8	1.9957(11)	Co1- N3	1.9345(11)
Fe1-N4	1.9432(11)	Fe2-N9	1.9417(11)	Co1-N4	1.9118(13)
Fe1 -N5	1.7000(12)	Fe2-N10	1.6989(11)	Co1-N5	1.7890(11)
N5-O1	1.1705(14)	N10-O2	1.1713(14)	N5-O1	1.1551(15)
O1-N5-Fe1	153.23(10)	O2-N10-Fe2	158.05(10)	O1-N5-Co1	125.97(9)
N1-Fe1-N2	81.67(5)	N6-Fe2-N7	81.48(5)	N1-Co1-N2	82.99(4)
N1-Fe1-N3	145.31(4)	N6-Fe2-N8	141.88(4)	N1-Co1-N3	168.75(4)
N1-Fe1-N4	95.63(5)	N6-Fe2-N9	95.14(5)	N1-Co1-N4	96.61(4)
N1-Fe1-N5	104.67(6)	N6-Fe2-N10	109.26(5)	N1-Co1-N5	96.49(5)
N2-Fe1-N3	90.30(5)	N7-Fe2-N8	89.89(5)	N2-Co1-N3	92.49(4)
N2-Fe1-N4	162.10(4)	N7-Fe2-N9	161.73(4)	N2-Co1-N4	152.26(4)
N2-Fe1-N5	100.96(5)	N7-Fe2-N10	101.52(5)	N2-Co1-N5	103.70(5)
N3-Fe1-N4	81.86(5)	N8-Fe2-N9	81.71(5)	N3-Co1-N4	82.60(4)
N3- Fe1-N5	109.99(5)	N8-Fe2- N10	108.84(6)	N3-Co1-N5	94.58(5)
N4- Fe1-N5	96.85(5)	N9-Fe2- N10	96.55(5)	N4- Co1-N5	103.90(4)

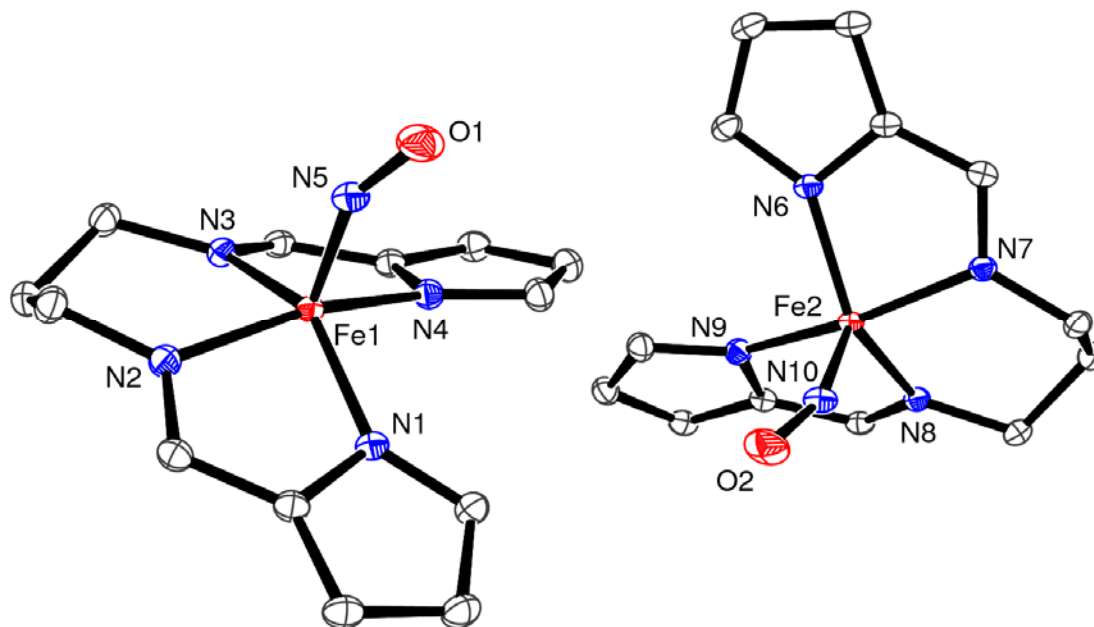


Figure S22. ORTEP views of the two independent molecules in the asymmetric unit of [Fe(LN₄)(NO)] (1) showing 50% probability thermal ellipsoids for all non-hydrogen atoms with the atom labeling scheme.

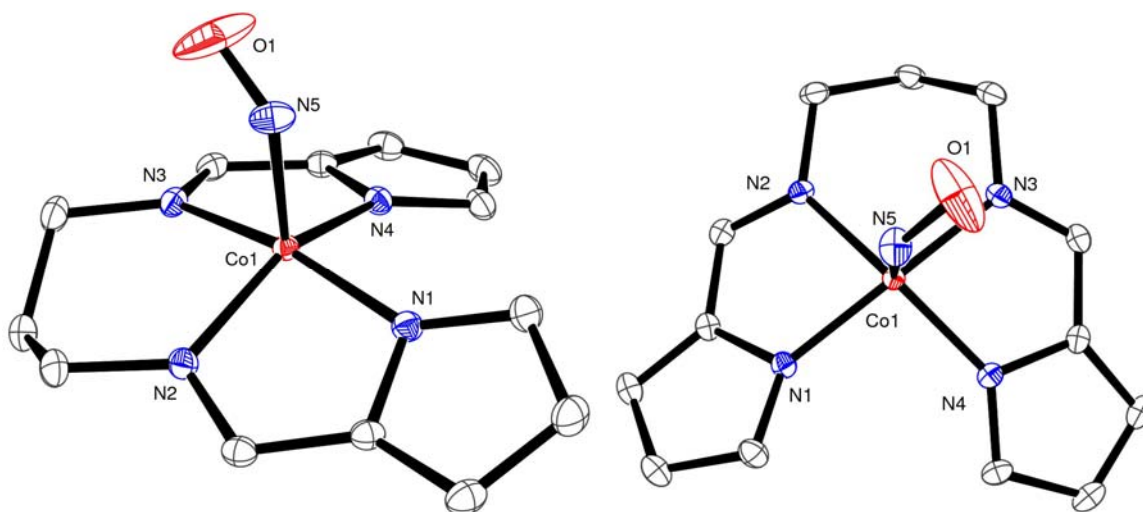


Figure S23. ORTEP views of [Co(LN₄)(NO)] (2) showing 50% probability thermal ellipsoids for all non-hydrogen atoms with the atom labeling scheme.

Computational Methods

The ADF2009¹¹ and Gaussian09¹² program systems were used in this study. The OLYP¹³ and PW91¹⁴ functionals with the Slater-type triple- ζ plus polarization (STO-TZP) basis sets were used with ADF and the B3LYP¹⁵ hybrid functional with the 6-311G(d,p) basis set was used with Gaussian09. Throughout, we used fine meshes for numerical integration of matrix elements as well as adequately tight criteria for geometry optimizations. The summary of the results of the DFT calculations are shown in Tables S3-S4 and Figure S24. Cartesian coordinates for the optimized geometries in two different conformations (A and B, see Table S3) of the M-N-O vector of **1**, **2**, and **3** are provided in Tables S5-S10.

On going from {FeNO}⁷ (**1**) to {FeNO}⁸ (**3**), the Mulliken charge (Table S4) decreases (in an algebraic sense) at Fe, the NO, and for a number of atoms on the equatorial ligand. The reduction in **3** is thus neither Fe- nor NO-centered. Second, unlike in 6C low-spin {FeNO}⁷ complexes, which carry substantial majority spin density on the NO, all three functionals examined indicate that the single unpaired spin of **1** is largely localized on the Fe. The calculations further indicate that the unpaired spin density on the NO in **1**, which is responsible for the observed hyperfine coupling in the EPR, is actually *minority* spin density. Although similar spin density profiles have been observed for nitrosylhemes, this is still a somewhat unaccustomed picture for inorganic chemists. There seems little doubt about the basic correctness of the picture, as high-level *ab initio* CASSCF calculations have reproduced it quite convincingly.¹⁶

Additional insights into the nature of {FeNO}⁸ complex **3** were obtained from calculations of singlet-triplet (S-T) splittings and electron affinities (EAs). Thus, OLYP/TZP calculations indicated an S-T splitting of 0.6 eV for **3**, essentially identical to those of {CoNO}⁸

complex **2** and of $\{\text{FeNO}\}^8$ and $\{\text{CoNO}\}^8$ porphyrin derivatives. Although hybrid functionals resulted in a small amount of broken-symmetry character (as evidenced by separation of α and β spin densities) across the $\{\text{MNO}\}^8$ unit, there was no evidence for a non-innocent equatorial ligand with any method. The OLYP calculations further indicated similar EAs of about 1.4 eV for both **3** and for the analogous $\{\text{FeNO}\}^7$ porphyrin, suggesting that barring difficult solubility problems, a variety of $\{\text{FeNO}\}^8$ derivatives should be isolable.

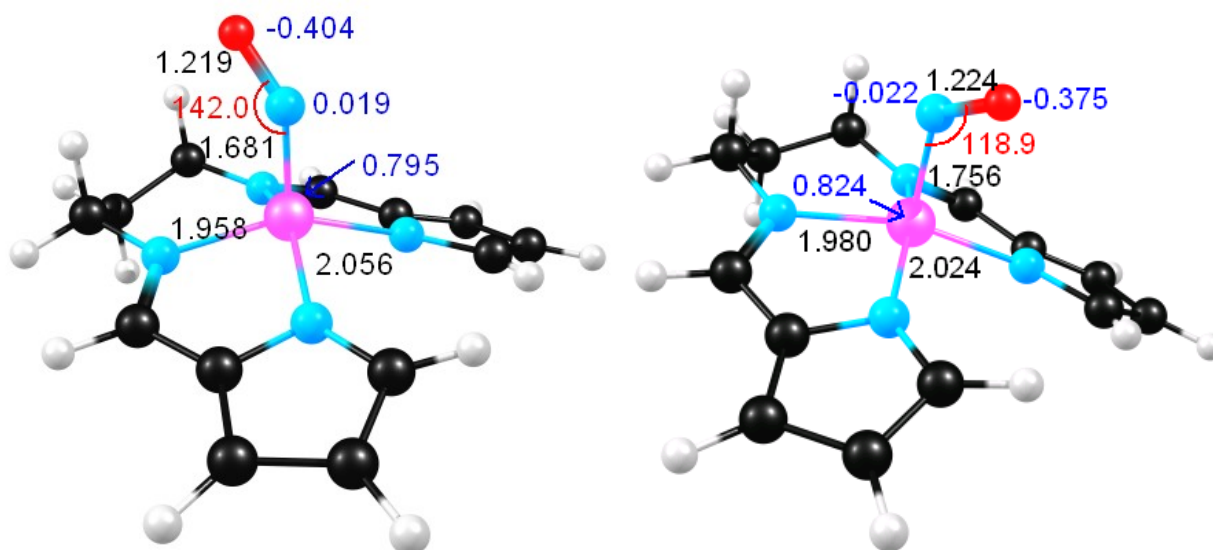


Figure S24. Geometry optimized (OLYP/TZP) equilibrium structures of conformation A (left) and conformation B (right) for $[\text{Fe}(\text{LN}_4)(\text{NO})]^-$ (anion of complex **3**) showing selected bond distances (Å in black) and angles (deg in red). For **3**, the conformation A versus B energy difference is 0.3 eV in favor of conformation A. Mulliken atomic charges are shown in blue. Atom labels: Fe (cyan); N (blue); O (red); C (black); H (white).

Table S3. Optimized OLYP/TZP geometry parameters for the two C_s minima of $\{\text{FeNO}\}^7$, (**1**) $\{\text{FeNO}\}^8$ (**3**), and $\{\text{CoNO}\}^8$ (**2**) complexes. Bolded parameters indicate the energetically-favored conformation of the M-N-O vector as displayed in the drawing. For **3**, the conformation A versus B energy difference is 0.3 eV while it is insignificant for **1** and **2**. For **1** and **2**, the bolded parameters represent what is also observed in the X-ray crystal structures.

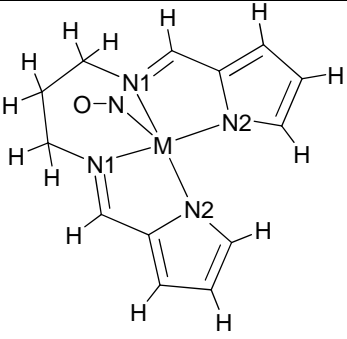
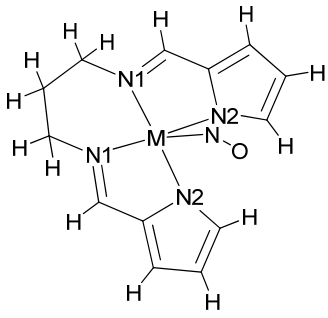
Complex/ Geom. param. (Å deg)	 Conformation A	 Conformation B
$\{\text{FeNO}\}^7$ (1)		
Fe-N(O)	1.685	1.690
N-O	1.186	1.183
FeNO	150.0	149.9
Fe-N1/N2	1.984/2.007	2.014/1.975
$\{\text{FeNO}\}^8$ (3)		
Fe-N(O)	1.681	1.756
N-O	1.219	1.224
FeNO	142.0	118.9
Fe-N1/N2	1.958/2.056	1.980/2.024
$\{\text{CoNO}\}^8$ (2)		
Co-N(O)	1.766	1.777
N-O	1.184	1.181
CoNO	125.2	122.8
Co-N1/N2	1.963/1.983	1.984/1.956

Table S4. Mulliken charges and spin populations for conformation B (see Table S3) of $\{\text{FeNO}\}^7$ (**1**) and conformation A of $\{\text{FeNO}\}^8$ (**3**) and $\{\text{CoNO}\}^8$ (**2**) of the optimized equilibrium structures. For $\{\text{MNO}\}^8$, the B3LYP data is for the broken symmetry solution.

Mulliken Charges	PW91			OLYP			B3LYP		
	M	N	O	M	N	O	M	N	O
$\{\text{FeNO}\}^7$ (1)	0.773	0.122	-0.250	0.894	0.099	-0.264	1.359	-0.168	-0.153
$\{\text{FeNO}\}^8$ (3)	0.693	0.045	-0.394	0.795	0.019	-0.404	1.228	-0.293	-0.308
$\{\text{CoNO}\}^8$ (2)	0.672	0.164	0.249	0.773	0.148	-0.251	1.218	-0.064	-0.093
Mulliken spin populations									
	M	N	O	M	N	O	M	N	O
$\{\text{FeNO}\}^7$ (1)	1.046	-0.038	-0.060	1.235	-0.127	-0.128	2.033	-0.528	-0.474
$\{\text{FeNO}\}^8$ (3)	0.000	0.000	0.000	0.000	0.000	0.000	1.375	-0.796	-0.488
$\{\text{CoNO}\}^8$ (2)	0.000	0.000	0.000	0.000	0.000	0.000	0.766	-0.431	-0.280

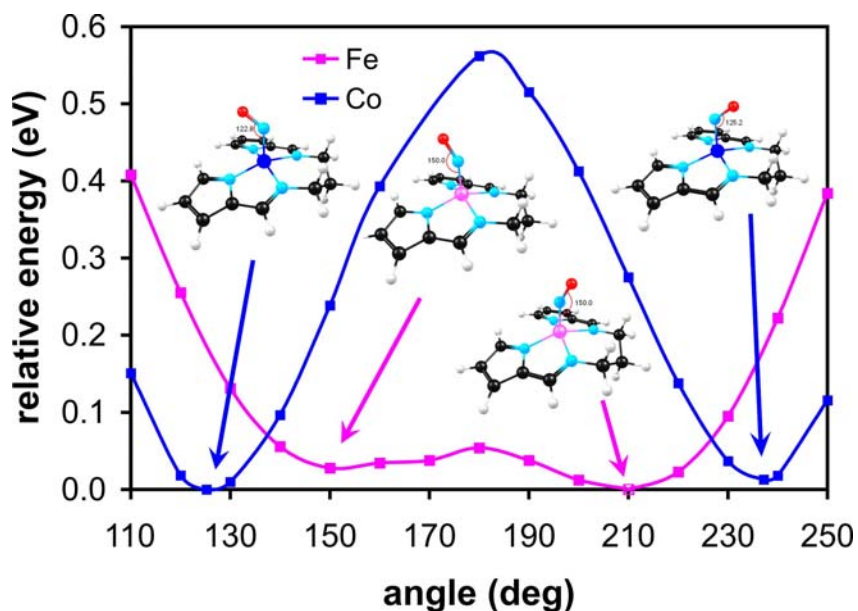


Figure S25. OLYP/TZP $\{\text{FeNO}\}^7$ (**1**) and $\{\text{CoNO}\}^8$ (**2**) bending potentials.

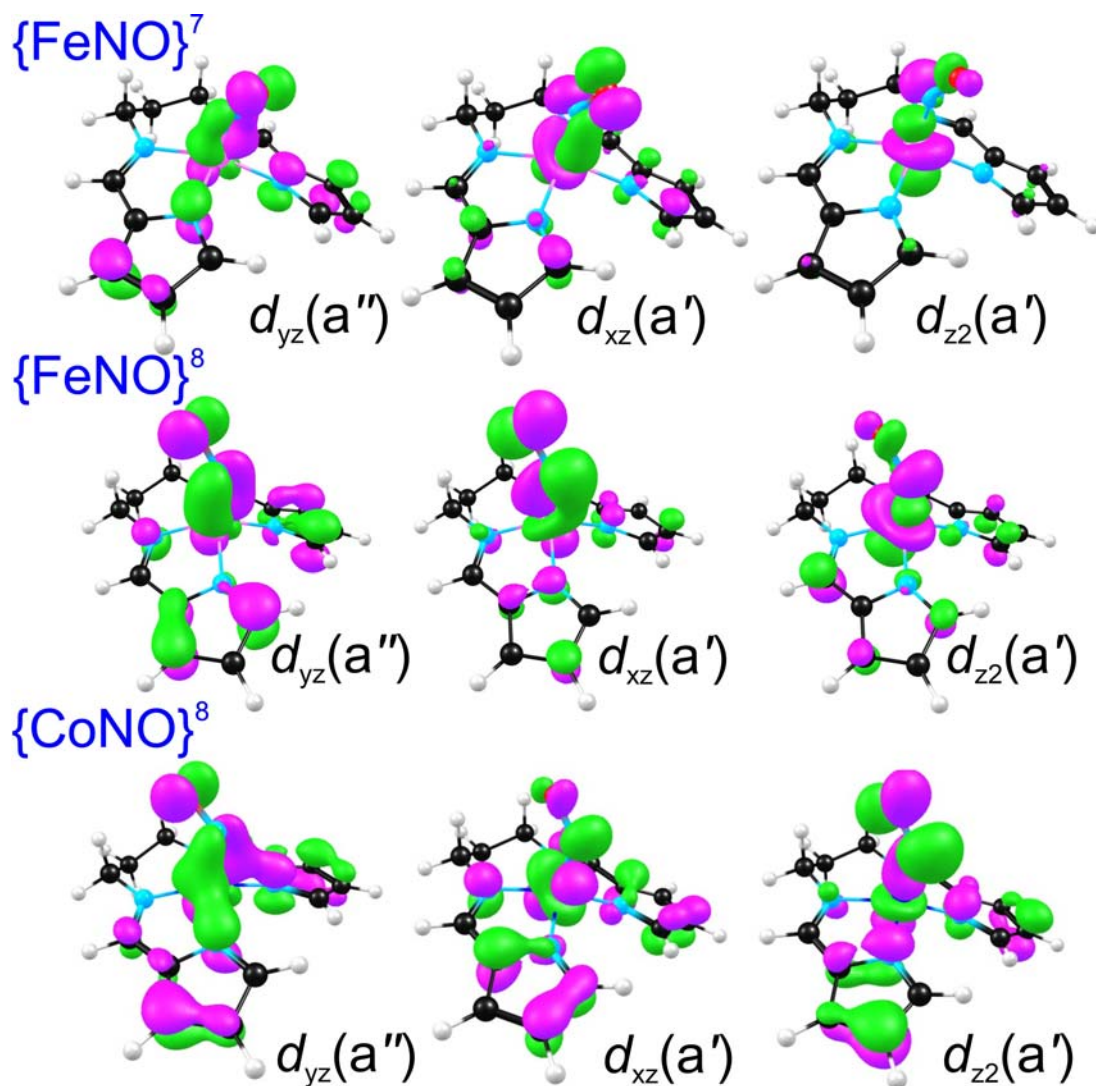


Figure S26. Metal(d)-NO(π^*) overlaps in the three HOMOs of optimized equilibrium structures derived from the experimental conformations of **1-2** (top and bottom, respectively) and theoretically determined **3** (middle) (see Table S3). Conformation B for $\{\text{FeNO}\}^7$ (**1**); conformation A for $\{\text{FeNO}\}^8$ (**3**) and $\{\text{CoNO}\}^8$ (**2**).

Table S5. OLYP/TZP optimized Cartesian coordinates (Å) for {FeNO}⁷ complex **1** (conformation A), $S = \frac{1}{2}$, C_s symmetry.

Fe	-0.149504000	-0.259063000	0.000000000
C	2.429277000	0.178577000	-1.799865000
C	2.632792000	0.566733000	-3.141202000
C	1.370373000	0.808659000	-3.687003000
C	0.449090000	0.549400000	-2.649997000
C	-0.949545000	0.534921000	-2.553214000
C	-2.925139000	0.053193000	-1.276716000
C	-3.461320000	0.701214000	0.000000000
C	-2.925139000	0.053193000	1.276716000
C	-0.949545000	0.534921000	2.553214000
C	0.449090000	0.549400000	2.649997000
C	1.370373000	0.808659000	3.687003000
C	2.632792000	0.566733000	3.141202000
C	2.429277000	0.178577000	1.799865000
N	1.116535000	0.173191000	-1.495788000
N	-1.481543000	0.171068000	-1.406357000
N	-1.481543000	0.171068000	1.406357000
N	1.116535000	0.173191000	1.495788000
N	-0.291842000	-1.937949000	0.000000000
O	-0.969159000	-2.910928000	0.000000000
H	3.184510000	-0.093344000	1.076366000
H	-1.584661000	0.801690000	3.401346000
H	-3.226403000	1.772482000	0.000000000
H	-1.584661000	0.801690000	-3.401346000
H	1.133719000	1.126978000	-4.695541000
H	3.592378000	0.658529000	-3.636305000
H	-4.554950000	0.604573000	0.000000000
H	3.184510000	-0.093344000	-1.076366000
H	-3.412355000	0.507510000	-2.149810000
H	-3.197924000	-1.012886000	-1.277562000
H	-3.197924000	-1.012886000	1.277562000
H	3.592378000	0.658529000	3.636305000
H	1.133719000	1.126978000	4.695541000
H	-3.412355000	0.507510000	2.149810000

Table S6. OLYP/TZP optimized Cartesian coordinates (Å) for {FeNO}⁷ complex **1** (conformation B), $S = \frac{1}{2}$, C_s symmetry.

Fe	-0.181419000	-0.262129000	0.000000000
C	2.385854000	0.061310000	-1.780170000
C	2.613743000	0.474810000	-3.106201000
C	1.365217000	0.790148000	-3.652866000
C	0.426063000	0.546613000	-2.632695000
C	-0.976207000	0.591956000	-2.548981000
C	-2.970179000	0.161789000	-1.280768000
C	-3.487677000	0.820417000	0.000000000
C	-2.970179000	0.161789000	1.280768000
C	-0.976207000	0.591956000	2.548981000
C	0.426063000	0.546613000	2.632695000
C	1.365217000	0.790148000	3.652866000
C	2.613743000	0.474810000	3.106201000
C	2.385854000	0.061310000	1.780170000
N	1.069479000	0.110107000	-1.482915000
N	-1.525975000	0.237897000	-1.412944000
N	-1.525975000	0.237897000	1.412944000
N	1.069479000	0.110107000	1.482915000
N	-0.149384000	-1.951776000	0.000000000
O	0.462700000	-2.963647000	0.000000000
H	3.121849000	-0.268127000	1.061670000
H	-1.589587000	0.889470000	3.403775000
H	-3.226281000	1.885669000	0.000000000
H	-1.589587000	0.889470000	-3.403775000
H	1.151117000	1.148650000	-4.652960000
H	3.579431000	0.536191000	-3.593913000
H	-4.583563000	0.752373000	0.000000000
H	3.121849000	-0.268127000	-1.061670000
H	-3.450738000	0.629741000	-2.151294000
H	-3.269175000	-0.898207000	-1.280860000
H	-3.269175000	-0.898207000	1.280860000
H	3.579431000	0.536191000	3.593913000
H	1.151117000	1.148650000	4.652960000
H	-3.450738000	0.629741000	2.151294000

Table S7. OLYP/TZP optimized Cartesian coordinates (Å) for {FeNO}⁸ complex **3** (conformation A), $S = 0$, C_s symmetry.

Fe	-0.014176000	0.343369000	0.000000000
C	2.357322000	-0.870605000	1.820484000
C	2.446163000	-1.298927000	3.159870000
C	1.155687000	-1.185400000	3.705189000
C	0.347794000	-0.684362000	2.662065000
C	-1.000928000	-0.283521000	2.552946000
C	-2.743806000	0.706813000	1.272707000
C	-3.440926000	0.226570000	0.000000000
C	-2.743806000	0.706813000	-1.272707000
C	-1.000928000	-0.283521000	-2.552946000
C	0.347794000	-0.684362000	-2.662065000
C	1.155687000	-1.185400000	-3.705189000
C	2.446163000	-1.298927000	-3.159870000
C	2.357322000	-0.870605000	-1.820484000
N	1.090945000	-0.506966000	1.510465000
N	-1.387248000	0.204130000	1.389136000
N	-1.387248000	0.204130000	-1.389136000
N	1.090945000	-0.506966000	-1.510465000
N	0.222474000	2.007994000	0.000000000
O	-0.385600000	3.064270000	0.000000000
H	3.153166000	-0.831803000	-1.088684000
H	-1.697643000	-0.352116000	-3.393058000
H	-3.494738000	-0.869941000	0.000000000
H	-1.697643000	-0.352116000	3.393058000
H	0.839987000	-1.416542000	4.717933000
H	3.340330000	-1.663234000	3.657480000
H	-4.472026000	0.611780000	0.000000000
H	3.153166000	-0.831803000	1.088684000
H	-3.336571000	0.401160000	2.149129000
H	-2.717543000	1.807137000	1.265352000
H	-2.717543000	1.807137000	-1.265352000
H	3.340330000	-1.663234000	-3.657480000
H	0.839987000	-1.416542000	-4.717933000
H	-3.336571000	0.401160000	-2.149129000

Table S8. OLYP/TZP optimized Cartesian coordinates (Å) for {FeNO}⁸ complex **3** (conformation B), *S* = 0, *C_s* symmetry.

Fe	-0.174544000	-0.219627000	0.000000000
C	2.403018000	0.012122000	-1.877487000
C	2.615260000	0.438435000	-3.205549000
C	1.355158000	0.793771000	-3.715489000
C	0.440321000	0.553621000	-2.668864000
C	-0.972114000	0.597154000	-2.558077000
C	-2.929090000	0.098295000	-1.283752000
C	-3.460147000	0.745673000	0.000000000
C	-2.929090000	0.098295000	1.283752000
C	-0.972114000	0.597154000	2.558077000
C	0.440321000	0.553621000	2.668864000
C	1.355158000	0.793771000	3.715489000
C	2.615260000	0.438435000	3.205549000
C	2.403018000	0.012122000	1.877487000
N	1.096072000	0.084540000	-1.545220000
N	-1.491305000	0.204436000	-1.416720000
N	-1.491305000	0.204436000	1.416720000
N	1.096072000	0.084540000	1.545220000
N	-0.472308000	-1.949758000	0.000000000
O	0.482744000	-2.715058000	0.000000000
H	3.142415000	-0.344041000	1.171134000
H	-1.606928000	0.914742000	3.392852000
H	-3.215925000	1.816687000	0.000000000
H	-1.606928000	0.914742000	-3.392852000
H	1.121906000	1.167057000	-4.708073000
H	3.570273000	0.484369000	-3.720178000
H	-4.557426000	0.658978000	0.000000000
H	3.142415000	-0.344041000	-1.171134000
H	-3.434726000	0.552196000	-2.152891000
H	-3.200245000	-0.970037000	-1.272488000
H	-3.200245000	-0.970037000	1.272488000
H	3.570273000	0.484369000	3.720178000
H	1.121906000	1.167057000	4.708073000
H	-3.434726000	0.552196000	2.152891000

Table S9. OLYP/TZP optimized Cartesian coordinates (Å) for {CoNO}⁸ complex **2** (conformation A), *S* = 0, *C_s* symmetry.

Co	0.107479000	-0.140096000	0.000000000
N	-1.172392000	0.091172000	1.497176000
N	1.415711000	0.255663000	-1.408441000
N	0.203453000	-1.903605000	0.000000000
O	1.206231000	-2.532702000	0.000000000
N	-1.172392000	0.091172000	-1.497176000
N	1.415711000	0.255663000	1.408441000
C	0.870047000	0.512451000	2.575437000
H	1.492562000	0.764381000	3.436875000
C	-0.528066000	0.433714000	-2.673729000
C	-2.482812000	-0.009194000	-1.794988000
H	-3.220272000	-0.279226000	-1.053482000
C	0.870047000	0.512451000	-2.575437000
H	1.492562000	0.764381000	-3.436875000
C	-2.708104000	0.279063000	-3.156845000
H	-3.671580000	0.281435000	-3.652796000
C	-1.461982000	0.566693000	-3.720986000
H	-1.244264000	0.832369000	-4.748894000
C	2.862894000	0.239342000	1.271823000
H	3.211127000	-0.804507000	1.260767000
H	3.317373000	0.720324000	2.148011000
C	2.862894000	0.239342000	-1.271823000
H	3.317373000	0.720324000	-2.148011000
H	3.211127000	-0.804507000	-1.260767000
C	3.346948000	0.933166000	0.000000000
H	4.444614000	0.923674000	0.000000000
H	3.026973000	1.982158000	0.000000000
C	-0.528066000	0.433714000	2.673729000
C	-2.708104000	0.279063000	3.156845000
H	-3.671580000	0.281435000	3.652796000
C	-1.461982000	0.566693000	3.720986000
H	-1.244264000	0.832369000	4.748894000
C	-2.482812000	-0.009194000	1.794988000
H	-3.220272000	-0.279226000	1.053482000

Table S10. OLYP/TZP optimized Cartesian coordinates (Å) for {CoNO}⁸ complex **2** (conformation B), *S* = 0, *C_s* symmetry.

Co	-0.172173000	-0.147932000	0.000000000
N	1.073749000	0.109372000	-1.486300000
N	-1.517825000	0.202013000	1.414976000
N	-0.340260000	-1.917189000	0.000000000
O	0.587674000	-2.648478000	0.000000000
N	1.073749000	0.109372000	1.486300000
N	-1.517825000	0.202013000	-1.414976000
C	-0.976934000	0.508483000	-2.569131000
H	-1.599465000	0.749018000	-3.434647000
C	0.425701000	0.486801000	2.652931000
C	2.390322000	0.078858000	1.775866000
H	3.131551000	-0.206211000	1.044346000
C	-0.976934000	0.508483000	2.569131000
H	-1.599465000	0.749018000	3.434647000
C	2.614830000	0.442381000	3.118990000
H	3.581215000	0.501745000	3.605385000
C	1.362973000	0.706719000	3.681485000
H	1.143419000	1.014506000	4.697056000
C	-2.956353000	0.070167000	-1.277723000
H	-3.215063000	-1.000382000	-1.271146000
H	-3.453641000	0.514664000	-2.150798000
C	-2.956353000	0.070167000	1.277723000
H	-3.453641000	0.514664000	2.150798000
H	-3.215063000	-1.000382000	1.271146000
C	-3.496137000	0.714716000	0.000000000
H	-4.588846000	0.609692000	0.000000000
H	-3.270069000	1.787964000	0.000000000
C	0.425701000	0.486801000	-2.652931000
C	2.614830000	0.442381000	-3.118990000
H	3.581215000	0.501745000	-3.605385000
C	1.362973000	0.706719000	-3.681485000
H	1.143419000	1.014506000	-4.697056000
C	2.390322000	0.078858000	-1.775866000
H	3.131551000	-0.206211000	-1.044346000

Mössbauer spectral studies

For zero-field Mössbauer studies, polycrystalline samples were measured at 298 K. All samples were prepared in a glovebox. Typically, a powdered sample (100 – 150 mg of complex) was ground to a fine powder with a mortar and pestle. These solid samples were then packed into a nylon sample holder, sealed in parafilm, and the spectrum acquired. For complex **3**, the nylon holder was sealed with epoxy resin due to slow leakage of air in parafilm-covered samples. A conventional transmission geometry Mössbauer spectrometer was used equipped with a constant acceleration Mössbauer Drive by WebResearch. The source was $^{57}\text{Co/Rh}$ maintained at RT. Velocity calibration was performed using a 6 μm -thick iron foil enriched in ^{57}Fe . Isomer shifts (δ) are reported with respect to metallic iron at room temperature (RT). Least-square fits were obtained using the Mössbauer fitting software WMOSS (WEBResearch, Medina, MN).

The Mössbauer spectrum of $[\text{Fe}(\text{LN}_4)(\text{NO})]$ (**1**) and $[\text{Co}(\text{Cp}^*)_2][\text{Fe}(\text{LN}_4)(\text{NO})]$ (**3**) at 298 K is shown in Figure S27 and Figure 6 of the main text, respectively. The spectrum of **1** exhibits an isomer shift (δ) = 0.11(3) mm/s and a quadrupole splitting (ΔE_Q) = 1.41(5) mm/s, analogous to other low-spin $\{\text{FeNO}\}^6$ type of complexes versus an $\{\text{FeNO}\}^7$ species.¹⁷ This unusually low value of δ could be indicative of the NO^+ nature of the nitrosyl in **1** and a potential explanation of the near linearity in the Fe-N-O bond. The Mössbauer spectrum of **3** is consistent with Fe-NO unit reduction affording δ = 0.51(3) mm/s and ΔE_Q = 1.41(5) mm/s and is comparable to the only other Mössbauer-characterized $\{\text{FeNO}\}^8$ system by Wieghardt that displays δ = 0.41 mm/s.¹⁸ This drastic increase in δ from **1**-to-**3** ($\Delta\delta$: 0.40 mm/s) indicates a change in the overall π -accepting ability of the ligand (δ increases with a decrease π -accepting ability of the diatom) as a similar trend is observed in the isostructural $[\text{Fe}(\text{cyclam-ac})\text{X}]^{n+/-}$ series (where X = NO^+ , NO, and NO^-).¹⁸

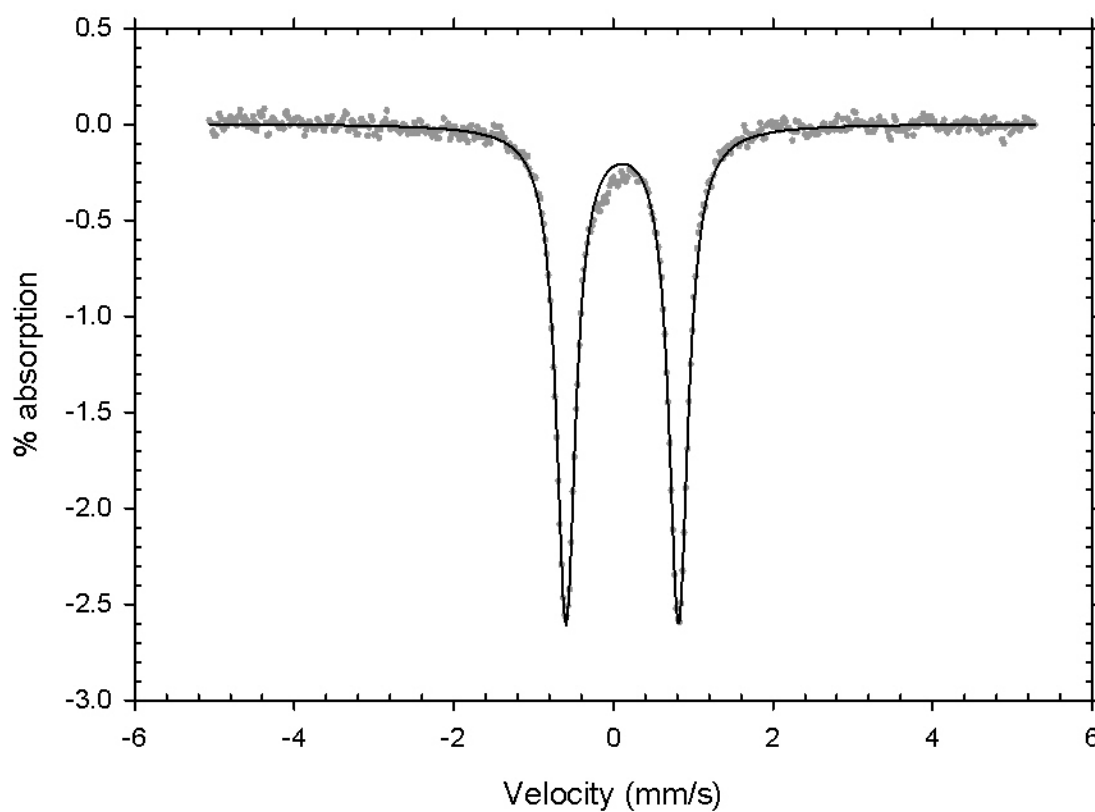


Figure S27. Zero-field Mössbauer spectrum of $[\text{Fe}(\text{LN}_4)(\text{NO})]$ (**1**) recorded at 298 K. The small deviation of the experimental data from the theoretical spectrum at ~ -0.2 mm/s indicates the presence of a small amount of impurity. The solid line shown is a least-square fit to the experimental data points of a simulated spectrum of one Fe species with $\delta = 0.11(3)$ mm/s and $\Delta E_Q = 1.41(5)$ mm/s.

References

- (1) Gill, N. S.; Taylor, F. B. *Inorg. Synth.* **1967**, *9*, 136.
- (2) (a) Evans, D. F. *J. Chem. Soc.* **1959**, 2003. (b) Sur, S. K. *J. Magn. Resn.* **1989**, *82*, 169.
- (3) Mason, J.; Larkworthy, L. F.; Moore, E. A. *Chem. Rev.* **2002**, *102*, 913.
- (4) (a) Antonini, E.; Brunori, M. *Hemoglobin and Myoglobin in their Reactions with Ligands*; North-Holland Publishing Company, Amsterdam, **1971**, p 19. (b) Romberg, R. W.; Kassner, R. J. *Biochemistry* **1979**, *18*, 5387.
- (5) *SMART v5.626: Software for the CCD Detector System*; Bruker AXS: Madison, WI, 2000.
- (6) Walker, N.; Stuart, D. *Acta Crystallogr.* **1983**, *A39*, 158.
- (7) Sheldrick, G. M. SADABS, Area Detector Absorption Correction, University of Göttingen, Göttingen, Germany, **2001**.
- (8) Sheldrick, G. M. SHELX-97, Program for Refinement of Crystal Structures, University of Göttingen, Göttingen, Germany, **1997**.
- (9) Sheldrick, G. M. SHELXTL 6.1, Crystallographic Computing System, Siemens Analytical X-Ray Instruments, Madison, WI, **2000**.
- (10) Burnett, M. N.; Johnson, C. K. ORTEP-III, Report ORNL - 6895; Oak Ridge National Laboratory: Oak Ridge, TN, **1996**.
- (11) Te Velde, G.; Bickelhaupt, F. M.; Baerends, E. J.; Guerra, C. F.; Van Gisbergen, S. J. A.; Snijders, J. G.; Ziegler, T. *J. Comput. Chem.* **2001**, *22*, 931.
- (12) Frisch, M. J.; Trucks, G. W.; Schlegel, H. B.; Scuseria, G. E.; Robb, M. A.; Cheeseman, J. R.; Montgomery, J. A., Jr.; Vreven, T.; Kudin, K. N.; Burant, J. C.; Millam, J. M.; Iyengar, S. S.; Tomasi, J.; Barone, V.; Mennucci, B.; Cossi, M.; Scalmani, G.; Rega, N.; Petersson, G. A.; Nakatsuji, H.; Hada, M.; Ehara, M.; Toyota, K.; Fukuda, R.; Hasegawa, J.; Ishida, M.; Nakajima, T.; Honda, Y.; Kitao, O.; Nakai, H.; Klene, M.; Li, X.; Knox, J. E.;

- Hratchian, H. P.; Cross, J. B.; Bakken, V.; Adamo, C.; Jaramillo, J.; Gomperts, R.; Stratmann, R. E.; Yazyev, O.; Austin, A. J.; Cammi, R.; Pomelli, C.; Ochterski, J. W.; Ayala, P. Y.; Morokuma, K.; Voth, G. A.; Salvador, P.; Dannenberg, J. J.; Zakrzewski, V. G.; Dapprich, S.; Daniels, A. D.; Strain, M. C.; Farkas, O.; Malick, D. K.; Rabuck, A. D.; Raghavachari, K.; Foresman, J. B.; Ortiz, J. V.; Cui, Q.; Baboul, A. G.; Clifford, S.; Cioslowski, J.; Stefanov, B. B.; Liu, G.; Liashenko, A.; Piskorz, P.; Komaromi, I.; Martin, R. L.; Fox, D. J.; Keith, T.; Al-Laham, M. A.; Peng, C. Y.; Nanayakkara, A.; Challacombe, M.; Gill, P. M. W.; Johnson, B.; Chen, W.; Wong, M. W.; Gonzalez, C.; Pople, J. A. Gaussian 03, revision C.02; Gaussian, Inc.: Wallingford, CT, 2004.
- (13) OPTX exchange functional: Handy, N. C.; Cohen, A. J. *Mol. Phys.* **2001**, *99*, 403.
- (14) Perdew, J. P.; Chevary, J. A.; Vosko, S. H.; Jackson, K. A.; Perderson, M. R.; Singh, D. J.; Fiolhais, C. *Phys. Rev. B* **1992**, *46*, 6671. Erratum: Perdew, J. P.; Chevary, J. A.; Vosko, S. H.; Jackson, K. A.; Perderson, M. R.; Singh, D. J.; Fiolhais, C. *Phys. Rev. B* **1993**, *48*, 4978.
- (15) LYP correlation functional: (a) Lee, C.; Yang, W.; Parr, R. G. *Phys. Rev. B* **1988**, *37*, 785. (b) Becke, A. D. *Phys. Rev. A* **1988**, *38*, 3098. (c) Becke, A. D. *J. Chem. Phys.* **1992**, *96*, 2155. (d) Becke, A. D. *J. Chem. Phys.* **1992**, *97*, 9173. (e) Becke, A. D. *J. Chem. Phys.* **1993**, *98*, 5648.
- (16) Radoń, M.; Broclawik, E.; Pierloot, K. *J. Phys. Chem. B* **2010**, *114*, 1518.
- (17) (a) Wyllie, G. R. A.; Scheidt, W. R. *Chem. Rev.* **2002**, *102*, 1067 and references therein. (b) McCleverty, J. A. *Chem. Rev.* **2004**, *104*, 403 and references therein.
- (18) Serres, R. G.; Grapperhaus, C. A.; Bothe, E.; Bill, E.; Weyhermüller, T.; Neese, F.; Wieghardt, K. *J. Am. Chem. Soc.* **2004**, *126*, 5138.